Untargeted Pixel-by-Pixel Imaging of Metabolite Ratio Pairs as a Novel Tool for Biomedical Discovery in Mass Spectrometry Imaging

Huiyong Cheng[1], Dawson Miller[1], Nneka Southwell[5], Joshua L. Fischer[2], Isobel Taylor[1], J. Michael Salbaum[3], Claudia Kappen[3], Fenghua Hu[4], Cha Yang[4], Steven S. Gross[1], Marilena D'Aurelio[5], and Qiuying Chen[1*]

[1]Department of Pharmacology and Brain and Mind Research Institute[5],Weill Cornell Medicine, New York, NY 10021

[2]Bruker Daltonics, Billerica, MA 01821

[3]Pennington Biomedical Research Center, Louisiana State University, Baton Rouge, LA 70808

[4]Cornell University, Department of Molecular Biology & Genetics, Ithaca, NY 14853-7202

*Correspondence should be addressed to:

Dr. Qiuying Chen, Weill Cornell Medicine, Department of Pharmacology, 1300 York Ave., New York, NY 10065. Phone: 212-746-6216. Email: qic2005@med.cornell.edu

Keywords

Metabolomics, mass spectrometry imaging; matrix-assisted laser desorption ionization mass spectrometry imaging, MALDI-MS, spatial metabolomics, metabolite ratio imaging, spatial metabotyping, tissue segmentation, metabolic pathway analysis

Abstract
Mass spectrometry imaging (MSI) is a powerful technology used to define the spatial distribution and relative abundance of structurally identified and yet-undefined metabolites across tissue cryosections. While numerous software packages enable pixel-by-pixel imaging of individual metabolites, the research community lacks a discovery tool that images all metabolite abundance ratio pairs. Importantly, recognition of correlated metabolite pairs informs discovery of unanticipated molecules contributing to shared metabolic pathways, uncovers hidden metabolic heterogeneity across cells and tissue subregions, and indicates single-timepoint flux through pathways of interest. Here, we describe the development and implementation of an untargeted R package workflow for pixel-by-pixel ratio imaging of all metabolites detected in an MSI experiment. Considering untargeted MSI studies of murine brain and embryogenesis, we demonstrate that ratio imaging minimizes systematic data variation introduced by sample handling and instrument drift, markedly enhances spatial image resolution, and reveals previously unrecognized metabotype-distinct tissue regions. Furthermore, ratio imaging facilitates identification of novel regional biomarkers and provides anatomical information regarding spatial distribution of metabolite-linked biochemical pathways. The algorithm described herein is applicable to any MSI dataset containing spatial information for metabolites, peptides or proteins, offering a potent tool to enhance knowledge obtained from current spatial metabolite profiling technologies.

Abbreviations
Mass spectrometry imaging (MSI); Fourier transform ion cyclotron resonance mass spectrometry (FT-ICR-MS); Matrix-assisted laser desorption/ionization mass spectrometry imaging (MALDI-MSI); Desorption electrospray ionization (DESI); Cytochrome C oxidase (COX); Knockout (KO); Wildtype (WT); Genome-wide association studies (GWAS); Metabolome-wide association studies (MWAS); Phosphatidylethanolamine (PE); Phosphatidic acid (PA); Lyso-phosphatidylethanolamine (LPE); Lyso-phosphatidic acid (LPA); Cyclic phosphatidic acid (CPA); Regions of interest (ROIs), N-Acetylaspartate (NAA); N-Acetylaspartylglutamate (NAAG); NAAG synthetase (NAAGS); N-Acetyltransferase 8 (NAT8); Fatty acid (FA); Phospholipase A1 (PLA1); Phospholipase A2 (PLA2); Docosahexaenoic acid (DHA); Arachidonic acid (AA); Monounsaturated fatty acid (MUFA); Polyunsaturated fatty acids (PUFA); Fatty acid synthase (FAS); Stearoyl-CoA desaturases (SCD); Glutaminase (GLS); Asparagine synthase (ASNS); AMP deaminase (AMPD); Carnosine synthase (CARNS); Hexose kinase (HK); Glutathione (GSH); Glutathione disulfide (GSSG) Glutathione peroxidase (GPX); Principal component analysis (PCA); Partial least square discriminant analysis (PLS-DA); Receiver operating characteristic curve (ROC) curve; Variable importance in projection (VIP); Hierarchical clustering analysis (HCA); Uniform manifold approximation and projection for dimension Reduction (UMAP)

Introduction

Recent developments in mass spectrometry imaging (MSI) enable spatial mapping of the relative distribution and abundances of proteins, peptides, lipids, small molecule metabolites, drugs and elemental isotopes in heterogeneous tissue sections[1] with resolution at, or near, cellular[2]. Hence, MSI has become a promising tool in the era of spatial-omics[3-15], especially at the single cell level[16]. Matrix-assisted laser desorption and ionization (MALDI) and desorption electrospray ionization (DESI) are the dominant modes of ionization for MSI. Regardless of ionization method, pixel size, and knowledge of structural identity, all MSI analyses provide pixel-by-pixel relative abundances of all detected charged molecular masses. Current MSI data processing tools provide 2D or 3D image data visualization as heatmaps from normalized pixel-by-pixel data of acquired mass spectra[17-20] and are currently limited to relative abundance data only.

Metabolite ratio imaging has been used in medical MRI spectroscopy to study metabolite distribution within tissue[21]. Additionally, targeted serum and urine metabolite ratios have aided assessment of genome-wide GWAS and MWAS association of metabolic traits by serving as proxies for enzymatic reaction rates[22-24]. Hypothesis-free testing of ratios between all possible metabolite pairs in tissue extracts analyzed by GWAS and MWAS have provided an innovative approach for discovery of new biologically meaningful molecular associations[25]. Furthermore, metabolite ratios have been used to construct large scale neural networks that improve statistical assessments and facilitate data interpretation[26]. Despite these promising applications, no computational approach has yet been reported that enables spatial imaging of all metabolite pairs in an MSI dataset.

To fill this gap, we developed an untargeted computational approach to image ratios of all detected metabolites in every pixel of an MSI experiment. While individual ion abundances in spatial metabolite profiling fail to inform on metabolic pathway activity, or on the identity of metabolic intermediates contributing to these pathways, pixel-by-pixel imaging of the ratio of an enzyme's substrate to its derived product offers an opportunity to view the distribution of functional activity for a given metabolic pathway across tissue. In this report, we use MALDI MSI data obtained from cryosections of murine embryos, brains, and a mitochondrial myopathy model of tissue derangements to demonstrate the application of ratio imaging to recognize both normal and pathology-associated regiospecific metabolic perturbations. We further show that ratio imaging minimizes systematic variations in MSI data introduced by sample handling and instrument drift, improves image resolution, enables anatomical mapping of metabotype heterogeneity, facilitates biomarker discovery, and reveals new spatially resolved tissue regions of interest (ROIs) that are metabolically distinct but otherwise unrecognized. Using murine embryo and hippocampus MALDI MSI data acquired at single cell spatial resolution, we showcase the potential of single cell metabolite ratios to probe metabolic enzyme activities, as well as the potential for integration with other datasets obtained using multiomic data acquisition platforms. Importantly, the algorithm for ratio imaging described should be applicable to spatial MS profiling of all sorts, including metabolites, peptides and proteins. This software package is being made available as a potent tool to enhance knowledge obtained from conventional spatial metabolite profiling analyses.

Materials and Methods

Sample preparation. Brain and adipose tissues from a mitochondrial myopathy model of cytochrome c oxidase assembly factor heme A:farnesyltransferase COX10 knockout (COX10 KO) and wildtype (WT) mice and adipose were frozen in liquid nitrogen and stored at −80 °C until processing. Entire mouse decidua dissected from pregnant females at gestation day 8.5 were embedded in 2% carboxymethylcellulose, frozen in liquid nitrogen, stored at -80°C, and sectioned at 12 µm nominal thickness. Brain cryosections were cut at 10 µm and adipose at 20 µm thickness (n=3 or 4 per group), mounted on conductive slides coated with indium tin oxide (ITO; (Delta Technologies; cat # CB-90IN-S111) and stored at -80°C. On the day of MALDI MS data acquisition, ITO-slides with tissue sections were transferred to a vacuum chamber and dried for 30 min prior to deposition of desired matrices for imaging: N-(1-naphthyl)ethylenediamine dihydrochloride (NEDC; 10 mg/ml in 75% methanol) for murine brain and E8.5 embryos; 1,5-diaminonaphthalene (DAN, 2 mg/mL in 50% acetonitrile) for murine COX10 KO adipose tissues, and 9-aminoacridine (9AA, 5mg/ml in 85% Ethanol) for murine hippocampus. All matrices were delivered using an HTX TM-Sprayer™ (HTX Technologies LLC, NC) with optimized spraying parameters for each individual matrix. Matrix-coated tissue sections were dried in vacuum desiccator for 20 min before MALDI MSI data acquisition in negative ion detection mode.

MALDI MSI data acquisition and processing. MALDI MSI data were acquired at raster width of either 10 µm or 80 µm using a 7T scimaX-MRMS mass spectrometer (Bruker Daltonics, USA) equipped with a SmartBeam II laser and a MALDI source. Peak-picked MALDI-IMS data were imported into SCiLS Lab 2023a software (SCiLS, Bremen, Germany) for image visualization. Compound identifications were assigned based on both accurate mass (<2 ppm mass accuracy) and isotope pattern matches to free source metabolite and lipid databases, including the Human Metabolome Database (HMDB), KEGG and LIPIDMAPs. An in-house R-code developed for the programmable Scils Lab Application Interface (Scils lab API) was used for fast export of raw pixel-by-pixel metabolite and unknown mass spectral abundance data from regions of interest (ROIs) and whole tissue sections. Missing abundance values for metabolite/feature at a given pixel was imputed as 1/5 of its minimum detected abundance among all pixels for that m/z species. Pixel-by-pixel metabolite ratios for detected metabolites/features were calculated using minimum-annotated pixel data. Differential metabolite ratios among ROIs were visualized in R and exported as either an image or .PDF file. Figure 1 depicts a schematic workflow using Scils Lab API for metabolite ratio imaging and associated multivariate analysis among ROIs. Notably, a series of Scils lab API R codes for ratio imaging visualization, data analysis, PCA and segmentation are available for download on GitHub. For MSI data acquired from other non-Bruker MS imaging instruments, R codes are also available to extract pixel data directly from .imzml file, a common data format for MS imaging, using Cardinal 3.0 free-source software and the resulting pixel data can be applied for ratio imaging (Figure 1).

Results

1. Generation of an untargeted spectral feature list for export of pixel data to enable downstream metabolite ratio analysis. Using Scils lab API, we sought to establish new data processing and analysis features for use in metabolite ratio imaging. To this end, we developed an R code that engenders fast export of raw or normalized pixel-by-pixel feature abundance data for all sections and/or regions of interest (ROIs) in an EXCEL.csv file format. A targeted feature list from metabolic pathways of interest can also be imported into Scils lab as .mir files, generated using either a Python program or a Scils lab feature list with manual ID annotation of peak-picked spectral data. Feature lists from multiple pathways

of interest can be saved for exclusive ratio imaging of these designated pathways. Once pixel data are available, a Scils lab license is no longer required for metabolite ratio imaging and downstream statistical analysis, except for label and spot image generation within the Scils lab environment. Notably, EXCEL format pixel data extracted from .imzml files of other vendor's proprietary MSI software are also amenable to the ratio imaging strategy described herein. Notably, pixel-by-pixel metabolite imaging data can also be co-registered with other omics imaging datasets obtained from a sequential serial cryosection, independent of the need for a Scils lab license.

Given the lack of need for proprietary software to export pixel-by-pixel data, an individual feature list provides MALDI-MS instrument/application flexibility. Additionally, considering each pixel as a replicate from a defined ROI, exported pixel data can be readily used with either vendor-specific or non-proprietary metabolomics data software platforms for biomarker discovery and multivariate spatial metabolomics analysis such as principal component analysis (PCA), partial least-squares discriminant analysis (PLS-DA), hierarchical clustering (HCA), ROC curve assessment, VIP scoring, and pathway enrichment.[27-39]. Figure S1 shows an exemplary conversion of ROI pixel data to formats compatible with import into MetaboAnlayst[27] and Agilent Mass Hunter Professional. For the presented data, brain outer cortex regions were selected for comparison between mitochondrial cytochrome oxidase 10 (COXKO) and WT (n=4 for each genotype) mice.

2. Annotating missing pixel abundance is required for MSI ratio imaging. Missing value annotation is conventionally employed for interpretation of omics data, including metabolomics[40-43]. Spatial metabolomics data acquired from MALDI and DESI MSI studies are subjected to missing value annotation when features are undetected in a given pixel. Given the differences in cell types and ionization efficiency/suppression across tissue regions, missing values are more common in spatial MSI than LC/MS data from the same tissue, especially in the case of FT-ICR-MS, which uses a peak-picking threshold to filter out the bulk of signal noise generated from Fourier data transformation. To prevent potential inclusion of a missing value as "zero" abundance for imaging data analyses that include ROI metabolite mean abundance comparisons, we annotate missing values with 1/5 the minimum value quantified in all pixels in which it was detected. Figure S2 A-B show the indistinguishable images of exemplary metabolites before and after missing value annotation[27]. Therefore, pixel-wise missing value annotated data was used for all statistical analyses, image plots, and metabolite ratio imaging described herein. To provide reciprocal and complementary images for easier ROI access and visualization, we consider images for both A/B and B/A ratios (Figure S2 C-D).

3. Pixel-by-pixel ratio imaging reduces cryosection preparation artefacts and improves data interpretation. Preparing cryosections from non-fixed and non-embedded tissues is a technically demanding procedure prone to sectioning artefacts[44]. Tissue freezing, cryo-cut temperature variation, section thickness irregularities and tissue storage can all affect imaging performance. Additionally, non-lipid small molecule metabolites suffer from smearing and/or diffusion during cryosection processing, including over the course of matrix deposition for MALDI-MSI. Pixel-by-pixel ratioing of metabolite/feature pairs offers the important advantage of reducing artefacts caused by non-uniform matrix coating of cryosections and other elements of sample processing, especially for slides containing multiple tissue cryosections. This is because as tissue cryosections are thaw-melted onto slides individually, the layout sequence results in variable waiting times for completion of the mounting process. Thus, individual cryosections undergo varying degrees of metabolically-active metabolite degradation, even at the typical -20°C cryotome operating temperature.

Figure 2A-C and Figure S2B compare images for lysophosphatidylethanolamines (LPEs 18:1, 20:4, 22:4, 22:6) on brain sections from COX10 KO and WT mice. Lysophospholipids contain a free hydroxyl moiety

in either the sn-1 or sn-2 position of the glycerol backbone and are generated by phospholipase-mediated (PLA1 and PLA2, respectively) hydrolysis of phospholipids. PLA1 hydrolyzes an ester bond at the sn-1 position, producing a saturated or monounsaturated fatty acid and a 1-lyso-2-acyl-phospholipid, while PLA2 preferentially hydrolyzes unsaturated fatty acids at the sn2 position, producing polyunsaturated fatty acids and a 2-lyso-1-acyl-phospholipid.

Notably, LPEs with polyunsaturated acyl chains of 20:4, 22:4 and 22:6 shown in Figure 2 predominantly originate from PLA1 action. As shown, images of these individual LPEs are relatively diffuse and variable among replicates of the same genotype (Figure 2 A-C). A relatively higher abundance of these species was imaged in cross-sections of the striatal ventral region of the brain, except for LPE 22:6 in COX10 KO brain, which was more abundant in the outer cortex. Note that 20:4 and 22:4 acyl chains are derived from the ω6 fatty acids arachidonic acid (AA) and adrenic acid, while 22:6 acyl chains originate from an ω3 fatty acid, docosahexaenoic acid (DHA).

Ratio images of LPE 20:4 and LPE 22:4 to LPE 22:6 indicate higher relative abundance of ω6 to ω3 LPEs in the striatum ventral region compared to the outer cortex (Figure 2 D-F), consistent with the ratio distribution of arachidonic acid to docosahexaenoic acid (Figure 2G). Compared to diffuse non-ratio images of individual LPEs, the ratio images of ω6 to ω3 LPEs show an enhanced brain structure with markedly sharper definition. Despite variable LPE values imaged between COX10 KO and WT brains, overall LPE ratios were unchanged between genotypes. Note that we purposely chose this set of non-ideal section quality and imaging data to demonstrate the clear benefit of ratio imaging in obviating potential sample processing artefacts, thus improving image quality for data interpretation.

4. Targeted metabolite ratio imaging reports spatial enzyme and pathway activities. For a given enzyme, pixel-wise specific enzyme activity can be inferred from pixel-by-pixel ratio imaging of substrate-product metabolite pairs. Examples of metabolite ratios that may serve as readouts for comparative enzyme activities include glutamine to glutamate for glutaminase (GLS), aspartate to asparagine for asparagine synthase (ASNS), aspartate to N-acetylaspartate for N-acetyltransferase 8 (NAT8L), inosine monophosphate (IMP) to adenosine monophosphate (AMP) for AMP deaminase (AMPD), lactate to pyruvate for lactate dehydrogenase (LDH), N-acetyl-aspartyl-glutamate (NAAG) to N-acetyl-aspartate for NAAG synthetase (NAAGS), carnosine to histidine for carnosine synthase (CARNS), hexose to hexose phosphate for hexose kinase (HK), glutamate to oxyproline for 5-oxoprolinase (OPLAH), and glutathione disulfide to glutathione for glutathione peroxidase (GPX).

For lipid related metabolites, ratios between different numbers of fatty acid double bonds for a given chain length (C16, C18, C20) would imply fatty acid desaturase (SCD) activity. Similarly, the fatty acid synthase (FAS) and PLA activities are reflected in the ratios of fatty acids with 2 carbon differences (C16 to C18, for example) and those of phospholipids to their corresponding lysophospholipids. Fatty acids are synthesized through metabolic pathways that include desaturation and elongation, sequentially producing a variety of long-chain saturated, monounsaturated, and polyunsaturated fatty acids (SFA, MUFA, and PUFA, respectively). Palmitic acid (FA 16:0) and stearic acid (FA 18:0) are the most common and abundant long chain saturated FAs in food and the human body. MUFAs synthesized from SFAs (via SCDs) are key components of phospholipids, triglycerides, and cholesterol esters that modulate cell membrane fluidity.

Obviously, pixel-by-pixel metabolite ratios are only possible for metabolite pairs detected and imaged within the same pixel of a given cryosection. MALDI-MSI using NEDC matrix and negative ion mode can detect all of the above-mentioned product-substrate pairs. Washing with acidic methanol significantly enhances the detection of phosphate-containing metabolites involved in energy metabolism[45].

Alternatively, using 9-Aminoacridine (9AA) as a matrix, purine and pyrimidine nucleotide mono-, di- and triphosphates can be imaged to obtain pixel-by-pixel ratios of nucleotides with different phosphate levels for assessment of relative phosphorylation status within a tissue.

Figure 3 demonstrates the benefit of imaging metabolically relevant metabolite ratio pairs in assessing regional gradients in enzymatic and metabolic pathways, as exemplified in E8.5 embryos at 10 μm (cellular) spatial resolution. Consistent with a role for the visceral yolk sac in providing nutrients, including glucose for embryo development, enhanced glycolytic activity was seen in the amnion and visceral yolk sac (Figure 3A-B). Furthermore, higher abundances of the desaturase product FA 18:1 relative to FA 18:0 (reflecting SCD activity) and of phophatidylethanolamine (PE) 38:4 relative to LPE 18:0 (reflecting PLA2 activity) are predominantly located in the allantois, head mesenchyme, and especially in the hindbrain neuroepithelium for FA 18:1 to FA 18:0 (Figure 3C, H). In contrast, the ratios of FA 16:0 relative to its elongation product FA 18:0, and DHA (ω3) relative to AA (ω6) fatty acids, showed opposite spatial distribution patterns (Figure 3D-E). Of note, similar ω3 to ω6 fatty acyl chain composition was also observed for LPEs (Figure 3F-G). Interestingly, PLA1 and PLA2 appear to have quite different compartmented activities among yolk sac, amnion, and head mesenchyme (Figure 3G-H). These data offer promising and useful information for study of compartmented metabolism during embryo development at the single cell level, demonstrating the power of metabolite ratio imaging in spatial assessment of metabolic activity.

As an additional example, we present mouse hippocampus MSI findings, which confirm that ratio imaging can resolve cell-type specific metabolic activity at cellular (10 μm) spatial resolution. Notably, neurons have higher energy requirements and prefer mitochondrial oxidative phosphorylation as their dominant energy source. In accord with this expectation, higher ATP/ADP, ADP/AMP, IDP/IMP ratios (Figure 3 J-L) are observed in neurons of mouse hippocampus, while indicators of oxidative stress (Figure 3I) and fatty acid synthesis (Figure 3P) were unchanged in neurons compared to other cell types. Elevated SCD and AMPD activities were also predominantly observed in neurons (Figure 3 M-N) compared to other cell types, consistent with SCD being a novel regulator of neuronal cell proliferation and differentiation and their reported immunocytochemical results[46]. Although a higher ratio of ω3 to ω6 fatty acids predicts improved hippocampus-dependent spatial memory and cognitive status in older adults[47], ratio imaging surprisingly shows that these neurons display a relatively lower level of DHA (ω3) to AA (ω6) fatty acids vs. other cell types in mouse hippocampus. Thus, ratio imaging findings have the potential to challenge existing concepts and guide further investigation.

Adipose tissues store body fat as neutral triglyceride and represent the chief energy reservoir in mammals. We previously reported that COX10 KO mice are typified by decreased white adipose stores, accelerated lipolysis with increased free fatty acid deposition and low leptin levels with decreased food intake[48]. We have since applied lipid and fatty acid ratio imaging to evaluate potential metabolic and enzymatic activities that may be responsible for the observed differences between COX10 KO and WT adipose tissue (Figure 4). As expected, distinct fatty acid and lipid profiles point to altered ω3 (DHA) to ω6 (AA) fatty acid composition (Figure 4A), fatty acid and lipid desaturation (Figure 4B-G), fatty acid synthesis (Figure 4H-J) and phospholipid hydrolysis (Figure 4K-L) in KO vs. WT adipose. Lower adipose ω3 to ω6 ratios have been associated with inflammation[49], obesity[50], altered gut microbiota[51,52] and other health problems[53,54]. These ratio imaging findings led us to speculate that the diminished ω3 to ω6 ratio in COX10 KO mice arises from an altered gut microbiome, supported by unpublished preliminary findings. This emergent hypothesis from ratio imaging analysis raises the clinically important possibility that supplementation of human COX10 mutant patients with ω3 fatty acids may effectively modify the microbiome to restore normalized adipose tissue composition and food intake. Taken together, these

results demonstrate the utility of ratio imaging as a valuable new MSI approach to probe for potential regiospecific changes in cellular metabolic activities.

5. Metabolite ratios uncover genotype-specific and spatially resolved tissue regions. Conventional MSI depicts relative spatial abundance of metabolite features in tissue regions. For defined structures in tissues such as brain, kidney and prostate, metabolite images can potentially recognize discrete tissue structures, under the condition that ionization efficiency and/or absolute abundance differences do indeed exist among these structurally defined loci. In contrast, pixel-by-pixel metabolite ratio imaging almost invariably resolves distinct tissue structures but also uncovers fine structure and anatomically unrecognized regions not revealed by individual metabolite imaging alone.

Using COX10 KO and WT mouse coronal brain sections as an example, we observed that individual glutamate, aspartate and glutamine distribution images failed to show a clear structural distribution, possibly due to diffusion of these hydrophilic metabolites (Figure 5A-C). However, ratio imaging revealed a much greater aspartate to glutamate ratio in an unusual "moon arc" region across the amygdala and hypothalamus relative to the rest of the coronal brain. Similar but different arc-like structures are encompassed within the ventral thalamus and hypothalamus, wherein a higher glutamate to glutamine ratio was observed (Figure 5D-E), while relative glutamine to aspartate abundance appears enriched in the striatum (Figure 5F). Thus, ratio imaging not only improves image quality for regional/cell-selective assessment of metabolite distributions but also offers an opportunity to discover new differentially metabolic regions with biological relevance. Note that the enrichment of aspartate to glutamate and glutamine to glutamate near the thalamus, nucleus accumbens (NAc) and hypothalamus (and visualization of their reciprocal ratio images) were robust and consistently reproduced in MALDI-MSI experiments using an independent cohort of COX10 KO and WT mouse brains (Figure 5G-H). Enrichment of glutamate to aspartate in the cortex region was further confirmed in horizontal and sagittal brain sections from random mouse brains (Figure 5I-J).

Considering the above, it is notable that aberrations in glutamate, glutamine and aspartate homeostasis are all implicated in neurological disease[55,56]. Aspartate serves as an amino donor for glial glutamate formation[57], and the hippocampal aspartate to glutamate ratio has been related to changes in brain glucose[58]. Glutamine is synthesized from glutamate and ammonia by the catalytic action of glutamine synthetase (GS) in glial cells of the brain, while it is also taken into neurons and generates glutamate and ammonia by the catalytic action of glutaminase. The glutamate-glutamine cycle is closely linked to cellular energy metabolism[56], and ratios between neurotransmitters (GABA, glutamine and glutamate) have been used in MRS studies to probe neurological disease mechanisms and progression[59,60]. Specifically, ratios among glutamine, glutamate and aspartate have been implicated in memory function[61], schizophrenia, depression, alcoholism and motivated performance via NAc[62]. Given the biological significance of these ratios, spatial ratio imaging can reveal previously unrecognized ROI and relative abundance ratio differences between disease and normal physiological states. In COX10 KO and WT brains, differential aspartate to glutamate and glutamine to glutamate ratios point to an interesting linkage between muscle health and brain neurotransmitter signaling: mitochondrial myopathy alters glutamine, glutamate and aspartate signaling near the NAc. This unusual finding is in accord with and supportive of our recent discovery of a coordinated multiorgan metabolic response that extends to the brain and is anticipated to play a role in human mitochondrial myopathy disease states[48].

6. Spatial correlation of ratio and non-ratio pixel-by-pixel data as an additional discovery tool. Combining pixel-by-pixel ratio and non-ratio data offers an additional tool for spatial metabolism discovery.

Despite that MALDI MSI is a soft ionization technique, it generates various adduct ion clusters and possible fragment ions from common neutral losses. Unknown non-ratio metabolite feature data in a given ROI can be combined with known metabolite ratios, pixel-by-pixel, to discover correlations between unknowns and metabolite ratios that inform on a specific enzyme activity or metabolic pathway. This application can reveal unrecognized but significantly correlated pathway metabolites and metabolite ratios, thus enabling recognition of unknown metabolites with relevance to specific pathways of interest.

Using COX10 KO and WT mouse adipose as an example, the unknown [M-H] 375.23059 was negatively correlated with the ratios of PA 36:4 to LPA 16:0 and PA 36:1 to PA 18:1, indicating that the abundance of this unknown metabolite may be positively associated with PLA1 and/or PLA2 activity (Table 1). Given that PLA1 and PLA2 generate different products, with PLA1 dominantly yielding unsaturated lysophospholipids and PLA2 yielding saturated lysophospholipids, an observed negative correlation of the unknown with LPA 18:1 to LPA 18:0 ratios hints that it may originate as a product of PLA2. Indeed, direct correlation of this unknown with lipid metabolites suggests it could be a reduction product of CPA 16:0 after loss of one oxygen atom, matching the formula $C_{19}H_{37}O_5P$ with 0.013 ppm mass accuracy. While it remains to be established that this unknown is a *bona fide* reduction product of CPA 16:0, the example illustrates how pixel-by-pixel correlations of unknown metabolite masses with metabolite ratios can aid potential discovery of pathway-relevant metabolites.

Another example of correlation-based discovery comes from consideration of COX10 KO and WT mouse brain sections, where calculating the Spearman correlation of combined pixel data from both individual metabolites and metabolite ratios revealed an unexpected positive association of $FeCl_2$ with the glutamate to glutamine ratio, along with other related metabolite ratios that include aspartate, NAA, glucose and glutathione (Table 2, Figure S3). Conversely, glutamine to glutamate ratios showed significant negative correlation with $FeCl_2$ and the above-mentioned metabolites (Table S1), suggesting these correlations are neither random nor an artefact of missing value annotation. Notably, free iron is recognized as a key mediator of glutamate excitotoxicity in spinal cord motor neurons[63]. Significant associations between peripheral markers of iron metabolism and glutamate with glutamine in relation to total creatine (Glx:tCr) concentration has been reported in female human brains[64]. Glutamate facilitates divalent metal transporter 1 (DMT1) flux and subsequent increases in brain free iron content[65]. A positive relation between iron and glutamate in the brain and other organs has also been reported[57,58,63,64,66,67].

Note that this correlation with $FeCl_2$ was observed in all brain sections regardless of genotype. Ferrous iron, measured as its chloride adduct when detected with NEDC matrix, likely arises from both free labile iron and protein-bound iron. Decreased $FeCl_2$ levels in combination with decreased glutamate in the cortex region of COX10 KO vs. WT brain is an unexpected but intriguing finding. While aging is associated with increased brain iron through cortex-derived expression of the iron regulatory hormone hepcidin[68], calorie restriction down-regulates hepcidin expression[69]. In accord with decreased Fe^{2+} and glutamate to glutamine ratio, COX10 KO mice exhibited decreased food intake and adopted a metabolic state resembling caloric restriction[48]. Collectively, pan-correlation of targeted metabolite ratios with non-ratio data serve as an additional imaging tool for data interpretation and hypothesis generation.

7. Metabolite ratios for PCA tissue segmentation in complex tissue sections. Spatial segmentation is a popular application in MSI to cluster regions with similar metabolite abundance profiles. Unsupervised MSI segmentation methods such as PCA, K-means, bisecting K-means and HCA are all often used to delineate underlying tissue structures from high-dimensional MSI data without prior knowledge of sample anatomical information. Most segmentation approaches rely on unsupervised clustering algorithms that

can readily result in the generation of biologically unrealistic tissue structures. Various algorithms for integrating partial or prior structural information with unsupervised clustering have been reported to improve segmentation results[70-76].

To date, tissue segmentation utilizing pixel-by-pixel metabolite ratio data for imaging differential metabolic zones has not been reported. We hypothesized that metabolite/feature ratios may generate more meaningful biologically relevant ROIs due in part to reduction of systematic experimental noise. Mouse brain sections serve as a good example for the utility of this approach. As expected, consideration of 10 different glutamate/glutamine related metabolites for PCA analysis (Table S2) with ratios involving the top 5 components generated an interesting arc-shaped region that encompasses the hypothalamus, striatum and NAc, while non-ratio metabolite data did not (Figure 6A). This metabolite ratio PCA result was used to provide an RGB image capturing the structure of the dataset by mapping the first of the five principal components. Apparently, this segmentation result captures and maintains the enriched arc-like regions shown previously in neurotransmitter ratio images (Figure 5D-E and G). Since glutamate plays key roles linking carbohydrate and amino acid metabolism via the tricarboxylic acid (TCA) cycle, as well as in nitrogen trafficking and ammonia homeostasis in the brain, this region likely exhibits unique glutamate-related metabolism and warrants further investigation. Likewise, a more defined outline of striatum and cerebellum in the coronal brain structure was obtained in PCA segmentation using the top 5 component metabolite ratios as well as 5 LPEs (Table S3) but was not observed with these 5 LPEs alone (Figure 6B).

As metabolite ratio data can segment tissue into novel ROIs, we considered the possibility that differential metabolite ratios can serve as markers to distinguish genotypes, either independently or when combined with individual metabolites. In COX10 KO and WT mouse brains, ratios among three neurotransmitter-related non-glutamate metabolites (glutamine, aspartate and homocarnosine) show clear differences within the cerebral cortex for glutamine to aspartate ratios (Figure 7A) and within the ventral striatum for homocarnosine to glutamine and homocarnosine to aspartate ratios (Figure 7 B-C).

The interrelationship of glutamine, aspartate and homocarnosine is shown in Figure 7D. Homocarnosine is a naturally occurring imidazole-containing dipeptide uniquely present in the brain, likely in a subclass of GABAergic neurons[77]. It is synthetized from γ-aminobutyric acid (GABA) and histidine via homocarnosine synthase (CARNS1) and can be hydrolyzed to histidine and GABA by carnosine dipeptidase 1 (CNDP1), which is exclusively expressed in brain (Figure 7D). Homocarnosine is recognized to play a role in mediating neuronal activity during satiation and starvation[78]. It is decreased in the brain during cold adaptation[79] and increased during alcohol intoxication[80]. Additionally, aspartate and glutamate can be exchanged across the inner mitochondrial membrane by mitochondrial carrier protein SLC25A12 (Aralar1), mainly distributed in brain and skeletal muscle for the transport of aspartate from mitochondria to cytosol, and in the transfer of cytosolic reducing equivalents into mitochondria as a member of the malate-aspartate shuttle[81]. Given the interrelationship of these three metabolites and their important roles in maintaining brain neurotransmitter pools, their ratios could report on neurotransmitter homeostasis. Indeed, it has been shown that brain function can be estimated from the ratio of glutamine to homocarnosine in cerebrospinal fluid[82]. An early report showed that homocarnosine is elevated in monkey brain in the setting of a protein-deficient diet, whereas aspartate and glutamate levels are unchanged[83]. Similarly, in COX10 KO and WT brains, we observed no difference in individual aspartate or glutamate levels (Figure 5 A-B), while striatal homocarnosine (Figure 7E) and glutamine (Figure 5C) were elevated. As COX10 KO mice displayed altered food intake, muscle mass and elevated starvation response[48], an elevated homocarnosine to glutamine and glutamine to glutamate ratio (Figure 5F) could

indicate increased synthesis of homocarnosine via the glutamine-glutamate-GABA axis. These results indicate that ratios among the three metabolites could serve as alternative markers to distinguish these murine genotypes.

To provide additional spatial detail, we performed PCA segmentation on COX10 KO and WT brains using ratio and non-ratio pixel data for homocarnosine, glutamine and aspartate with the goal of learning whether differential ROIs exist for these genotypes. In this PCA segmentation, the overview RGB image maps the first three principal components to the red, green and blue channels respectively. Comparing PCA overview images from ratio (Figure 7F) to non-ratio (Figure 7G), PCA results from ratios showed cyan blue located in larger areas of striatum and thalamus regions in KO relative to WT brains, while non-ratio PCA did not. These results reveal distinguishable differences in abundance in the cyan region of the KO and WT brain regarding interconversion and homeostasis of the three neurotransmitter-relevant metabolites. Therefore, metabolite ratios could serve as better candidates for ROI-based disease metabotyping.

8. UMAP using metabolite ratios enables spatial metabotype mapping and recognizes novel ROIs. Unlike PCA analysis, which builds on a linear dimension reduction algorithm, uniform manifold approximation and projection (UMAP) is a relatively newer non-linear dimension reduction algorithm often used to visualize complex dataset while preserving local structure. UMAP projects dimensionally reduced data into 2D or 3D scatterplots. Samples close to each other in the scatterplot have similar fingerprints, while samples further away have progressively different profiles. It is often used in combination with other clustering algorithms such as HCA and K-mean clustering to identify subgroups in the projected space. UMAP has been widely used for omics data interpretation to find internal structure in mixed datasets, as well as for disease subtyping, single cell bioogy[84-86] and various molecular imaging applications.

Since metabolite ratio segmentation using PCA is less prone to section preparation artefacts in MALDI-MSI and enables genotype-specific tissue segmentation (Figure 7F), we sought to assess whether metabolite ratio UMAPing and clustering could generate novel ROIs that enable new spatial metabotype mapping beyond that obtained from consideration of individual metabolites. UMAP analysis of ratios for 5 LPEs in COX10 KO and WT murine brain sections, followed by K-mean clustering, showed much more defined and biologically relevant ROIs than those derived from non-ratioed LPEs (Figure 8) that resemble PCA segmentation results (Figure 6B). This UMAP analysis used 9 neighbors with 2 Euclidean components as metric measurements of similarity. Figures S4-5 show the nine segmented ROIs from ratio and non-ratio UMAP and K-mean clustering analyses, along with scatterplots of the first 2 UMAP components (V1 vs. V2), projecting the distribution and similarity of each of 9 segmented ROIs. While non-ratio segmented ROIs did not provide comparable and confident ROIs among replicates (Figure S4), the ratio-segmented data indicate a distinct LPE profile between the outer cortex (ROI 3), cortex (ROI 8), ventral thalamus (ROI 5) and striatal regions (ROI 2) (Figure S5). These ROIs generated by UMAP metabolite ratios enable visualization and a reproducible comparison of lipid metabolite and/or ratio abundance among these irregular and difficult-to-draw (i.e. with imprecise anatomical definition) regions. In addition, they provide unique ROIs for pixel-by-pixel metabolite correlation with other previously mentioned multivariate analyses (Table 1, Figure S1)

Differences in metabolite abundance among ROIs can be difficult to visualize if the image color scale is set too wide. ROI images are better visualized by applying a relative image abundance scale set to a discrete ROI, rather than the entire tissue section. UMAP segmentation using ratios provides novel ROIs for such purpose. For example, murine brain imaging results showed decreased aspartate to NAA ratios

visualizable in almost all 8 ROIs investigated with COX10 KO relative to WT, suggesting overall diminished expression or activity of NAT8L, the neuronal enzyme that produces NAA from acetyl-CoA and aspartate (Figure S6 A-H). Moreover, NAAG, the most abundant dipeptide in the brain, can be synthesized from NAA and glutamate by NAAG synthase. NAAG to NAA and aspartate ratios were greater in ROI 7 of KO compared to WT brain (Figure S6 I-J), suggesting elevated NAAG synthase activity in this defined region. Of note, NAT8L mRNA oxidation is linked to neurodegeneration in multiple sclerosis[87] and overexpression-induced vulnerability to depressive behavior in mice[88]. NAAG functions as a retrograde neurotransmitter and is released in response to glutamate, providing postsynaptic neurons with a feedback mechanism to inhibit excessive glutamate signaling[89]. Therefore, elevated NAT8L activity, indicated by an increased NAA to aspartate ratio, is consistent with observations that COX10 KO mice are less mobile and relatively inactive compared to WT. Reviewing the non-ratio images of these metabolites, NAAG is mainly enriched near ROI 7 visualized in whole section images (Figure S7 A), consistent with higher abundance of NAAG, NAA and glutamine imaged exclusively in COX10 KO ROI 7 (Figure S7 B-D). These changes contrast with the decreased aspartate and unchanged glutamate levels imaged in ROI 7 of KO brains (Figure S7 E-F). Therefore, we infer that the COX10 KO brain exhibits increased NAA and NAAG syntheses as feedback to inhibit excessive glutamate signaling. In contrast, glutamate within the NAc showed no change compared to WT, potentially due to excess glutamate being used for synthesis of glutamine and NAAG, which are elevated in KO ROI 7 (Figure S7 C-D). Consideration of these UMAP findings exemplifies the applicability of this strategy for MSI data interpretation.

UMAP derived ROIs can be applied to survey metabolite abundances, pixel-by-pixel, for correlation analysis in ROIs from a large combined dataset that includes metabolite ratio and non-ratio pixel data, as shown previously for whole tissue sections (Tables 1 and 2A). When correlation is narrowed to a specific ROI and genotype, regional correlation results can be very different from global correlations. Figure S8 show pixel-by-pixel correlation of the glutamine to glutamate ratio, along with a compendium of all detected metabolites and ratios contained in a UMAP-generated ROI 7, comparing COX10 KO and WT brain. For improved correlation plot visualization, only significant correlations with Spearman correlation coefficients >0.4 are presented in Figure S8. Glutamate to glutamine ratio positively correlated, while negative correlations were observed for glutamate/NAAG and NAAG/NAA in both WT and KO ROI 7 (Table S5). These findings are consistent with existing knowledge that NAAG synthesis inhibits excess glutamate signaling.

Given that LPE ratios can be used as a tool for brain segmentation and to overcome variations in section quality, we asked if UMAP with the same 5 LPE ratios can similarly be applied for other types of brain section ROI segmentation. As predicted, UMAP generated ROIs consistent with brain anatomy in two separate experiments depicted by horizonal and sagittal brain sections (Figure S9). Collectively, UMAP analyses using metabolite ratio imaging provide a novel and robust tool to spatially-map tissue microenvironments, revealing matched localized differences among test groups.

Discussion

Analyses that utilize metabolite ratios are not a new concept in omics investigations, particularly for applications that involve medical MRI spectroscopy-generated imaging data. Notwithstanding, an unbiased strategy and application of pixel-by-pixel imaging of targeted and untargeted metabolite ratios for MSI data interpretation has been lacking. We demonstrate that ratio imaging adds a powerful new

tool to mitigate sample preparation artefacts, to spatially metabotype tissue microenvironments, and to reveal spatially distinct functional variations in enzymatic and metabolic pathway activities.

Metabolite ratio imaging can uncover previously unrecognized biology, as exemplified here for the pixel-by-pixel distribution and metabolic interplay among neurotransmitter-related brain metabolites. Glutamate, glutamine, aspartate, histidine, homocarnosine and GABA are all well-recognized brain metabolites that contribute to fundamental brain activities, including synaptic transmission and energy production. Their ratios are tightly regulated for maintaining proper brain function and vary across different regions of the brain and under different physiological conditions. Disturbance of these ratios can be deleterious to neurotransmission and overall brain health. Imaging of ratios among these and all other metabolites engenders a novel mapping tool that may point to localized segmentation of metabolic activities not recognized by imaging individual metabolites. Considering ratios as proxies of enzyme reaction rates between substrate and product, ratio-derived ROIs along with their ratio and non-ratio abundances offer a novel strategy for study of disease pathophysiology, biomarker discovery and identification of new therapeutic targets (Figures 5-7).

As described, untargeted pixel-by pixel ratios can be derived from all detected mass spectral features, irrespective of whether the features have known structural identities. Combined with non-ratio feature data, information-rich metabolite ratio datasets offer great potential for association with other imaging or spatial omics data. Notably, generation of metabolite ratio datasets can be performed using the described R-code algorithm and applied pixel-by-pixel to individual metabolite features that have been incorporated into an EXCEL.csv format file with spot ID and pixel axis positional information. Furthermore, R codes for generating pixel data directly from .imzml files provide a convenient way to perform spatial ratio analysis for all types of MSI experiments. For pixel data with ≤10 µm raster width, single cell spatial imaging and omics data can ideally be associated with untargeted metabolite/feature ratio data to achieve single cell multiomics metadata integration. For this purpose, a P-gain can be applied to filter out significantly correlated associations, as previously described for some well-established GWAS and MWAS association studies[22-25]. A potential challenge for single cell metabolomics spatial data interpretation lies in possible concerns regarding metabolite data co-registration with anatomical or other single cell omics datasets. Notably, when datasets are obtained from serial sections, a mere 10 µm shift could result in cell layer disparities.

Combining ratio and non-ratio pixel data offers a powerful new tool to survey significant but unappreciated global correlations between metabolites ratios (both structurally defined and undefined) in distinct ROIs that are revealed by metabolite ratio tissue segmentation. Among other unexpected findings, we demonstrate that an elevated glutamine to glutamate ratio is observed in COX10 KO brain compared to WT within the NAc and that this ratio positively correlates with ferrous iron levels and Nat8L enzymatic activity (inferred from NAA to aspartate ratios, Table 2, Figures S3 and S7). These associations were previously unrecognized but are consistent with a whole-body feed-forward action of mitochondrial myopathy on levels of brain leptin, corticosteroids and neurotransmitter signaling[48].

Applying targeted and untargeted metabolite ratios for PCA and UMAP tissue segmentation generates novel and artefact-free ROIs linking proxy metabolic activity. One limitation for MSI ratio data interpretation is that the coverage of known metabolite structures and pathways is considerably less (typically 200-300 structurally identified species) than for LC/MS analyses. It is important to note that combined ratio and non-ratio data can also be used for segmentation. However, segmentation results using combined ratio and non-ratio data may be confounded by artefact-prone non-ratio metabolite data and thus not as clean as those using ratio alone. We speculate that combining metabolite ratios from different metabolic pathways may segment tissue with ROIs more representative of real metabotypes.

In summary, we anticipate targeted and untargeted metabolite ratio imaging to provide a powerful add-on tool for MSI experiments, revealing otherwise hidden information in acquired datasets. These ratios may serve as potential new biomarkers to distinguish anatomically distinct metabolic tissue regions and uncover otherwise unrecognized differences in either physiological cell function or from differing cellular responses to drug treatments and disease states. This ratio imaging strategy can be further extended to image pixel-by-pixel fractional abundance of isotopologues for targeted and untargeted MALDI-MSI stable isotope tracing. When coupled with the FT-ICR high resolution mass spectrometer, simultaneous imaging of isotopologue incorporation is possible for tracing molecules containing mixed stable isotope elements (e.g. ^{13}C, ^{15}N, ^{2}H, ^{18}O, ^{34}S).

Acknowledgements

We are thankful for Drs. Tal Nuriel, Eileen Ruth Torres, Li Gan for sharing mouse brain images used in this paper. NIH support by 1S10OD023652 (SG) for WCM's Ultra-high Resolution MALDI-FT-ICR Imaging Core Facility. NIH 5 R01 AR076029-03A1 (QC and MD), R21 NS118233-01A1 (QC and MD), R21 ES032347(QC).

Author contributions

HC, DM, NS, JF, IT, JMS, CK, CY and FH; MALDI MS sample preparation and data analyses, HC, SSG, MD and QC; conceptualization, HC and QC; writing.

Conflicts of Interest

None

Figure legends

Figure 1. Schematic workflow of metabolite ratio imaging using pixel data from Bruker Scils Lab API or imzml file from any MSI data source. For Scils lab MSI data, the execution of R codes starts with connecting a local Scils lab session project in R studio. Installation of Scils lab is required for this connection. After pixel data for a feature list is generated and exported as an EXCEL csv file, Scils lab installation is not required for downstream ratio imaging and data analysis, except for the potential writing of a spot image with labels back to Scils lab. For other types of MSI data, R code execution extracts pixel data from imzml file for subsequent ratio imaging and analysis.

Figure 2. Pixel-by-pixel ratio image visualization reduces cryosection preparation artefacts and enables spatial metabolic discovery in COX 10 KO mouse brain (left 4 sections) compared to WT (right four sections). Panel A-C: blurry and diffused images of LPEs with ω3 (A-B) and ω6 (C) polyunsaturated fatty acyl chains; Panel D-F: sharper ratio images of ω3 fatty acid containing LPE 20:4 and LPE 22:4 to ω6 fatty acid containing LPE 22:6; Panel G: ratio image of ω6 arachidonic acid (FA 20:4) to ω3 docosahexaenoic acid (FA 22:6) is consistent with the identified abundance ratio distributions for LPE 20:4 and LPE 22:4 to LPE 22:6.

Figure 3. Metabolically relevant metabolite ratio pairs that probe enzymatic and metabolic pathway activity in E8.5 mouse embryo cryosections and mouse hippocampus at 10 μm spatial resolution. Panel A: annotated drawing of E 8.5 embryo tissue, derived from the section adjacent to imaged section. Panel B-H: Ratio of substrate/ product pairs of glycolysis, fatty acid and lipid metabolism that imply compartmented activities for hexokinase (B), fatty acid desaturation (C), fatty acid chain elongation (D), fatty acid composition (E-F) and phospholipase activity (G-H) in E 8.5 embryos.

Figure 4. Altered fatty acid and lipid metabolism probed by ratio imaging in adipose tissue from COX 10 KO vs.WT mice. COX 10 KO, left 4 sections; WT, right 3 sections. Imaging data was acquired at 80 μm spatial resolution. Panel A: Decreased abundance ratio of FA 22:6 (DHA, ω3 fatty acid) to FA 20:4 (AA, ω6 fatty acid) in COX 10 KO adipose tissue. Panel B-C: Decreased fatty acid FA 16:0 and FA 18:0 desaturation in COX 10 KO adipose. Panel D-E: Decreased desaturated fatty acid abundance ratios for lysophospolipids and phospholipids in COX 10 KO adipose tissue. Panel H-J: Elevated fatty acid synthesis inferred by free fatty acid and phospholipids ratios, considering FA 18:0 to FA 16:0 (H-I) and FA 20:1 to 18:1 (L) in COX 10 KO adipose. Panel K-L: Elevated PLA2 (K) and PLA1(L) activities implied by the elevated ratio of Lyso PA to PA in COX 10 KO adipose.

Figure 5. Ratio imaging uncovers novel mouse brain regions with genotype-specific and spatially resolved ratios of aspartate, glutamate and glutamine. Panel A-C: images of glutamine, glutamate and aspartate in coronal sections of COX 10 KO (left 4 sections) and WT (right 4 sections) mouse brains. Panel D-F: Differential abundance ratios of aspartate, glutamate and glutamine observed in defined regions of the COX 10 KO and WT brains. Panel G-H: Reciprocal and differential aspartate to glutamate ratio and Arc-like NAC containing region was repeated in a separate group of COX 10 KO (left 4 sections) and WT (right four sections) mouse brains. Panel I-J: Enrichment in the glutamate to aspartate ratio in the cortex region of mouse brain, as revealed in horizonal and sagittal sections.

Figure 6. PCA segmentation of mouse brains comparing ratio and non-ratio metabolite pixel data. Panel A: PCA considering the top 5 components from ratios of 10-glutamate related metabolites that reveal an unanticipated arc-like regional distribution within the hypothalamus, striatum and NAc, that is not detected

by consideration of only non-ratio metabolite data. Panel B: PCA considering the top 5 components 5-LPE metabolites showing fine brain structure that is not fully represented by only non-ratio metabolite segmentation.

Figure 7. Metabolite ratios for segmentation and biomarker discovery in segmented ROIs. KO: right 4 sections; WT: left 4 sections. Panel A-C: Ratio images of homocarnosine, glutamine and aspartate in. Panel D: Enzymatic regulation and interconversions among brain glutamine, aspartate and homocarnosine. Panel E: Image of homocarnosine. Panel F: PCA with top 5 components and using ratios of homocarnosine, glutamine and aspartate shows differential ROI abundance shown in cyan blue in larger area of striatum, thalamus hypothalamus regions in KO compared to WT. Panel G: PCA with top 5 components and using homocarnosine, glutamine and aspartate pixel data show indistinguishable ROIs between genotypes.

Figure 8. UMAP analysis using 5 LPEs ratio followed by K-mean clustering on COX KO and WT brain sections shows a much cleaner and biologically relevant ROIs compared to those of LPE non-ratio. Panel A: UMAP clustering using ratios of 5 LPEs. Panel B: UMAP clustering using 5 LPE pixel data. The list of 5 LPEs is shown Table S3. Nine neighbors, 2 components with Euclidean distance as metric measurement of similarities were used in this UMAP analysis.

Supplemental figures

Figure S1 Application of pixel-by-pixel exemplary MALDI MS imaging data to metabolomics multivariate analysis using free or commercially available software package. Panel A: ROIs of COX 10 KO and WT brain outer cortex; Panel B: PLS-DA score plot showing classification of COX 10 KO and WT cortex pixels using Metaboanalyst 5.0 (https://www.metaboanalyst.ca/MetaboAnalyst/ModuleView.xhtml). Panel C: Variable importance in projection (VIP) scores of metabolites from PLS-DA shown in panel B. The colored boxes on the right indicate the relative concentrations of the corresponding metabolite in COX 10 KO and WT. Panel D: Matched pathways showing p values from the pathway enrichment analysis and pathway impact values from the pathway topology analysis. Differential metabolites imaged in cortex of COX 10 KO vs WT brain and metabolite quarries from KEGG mouse metabolic pathway were used in this analysis. Panel E: Metabolite set enrichment analysis showing enrichment ratio of metabolic pathway metabolites. Differential metabolites from cortex of COX 10 KO vs WT and the Small Molecule Pathway Database (SMPDB) were used for this analysis. The enrichment analysis resembles gene set enrichment analysis in transcriptomics. Panel F: Metabolite correlation heatmap generated from differential metabolites in cortex of COX 10 KO and WT. Metaboanalyst 5.0 was used for analyses shown in panel B-E and Agilent MassProfiler Professional 15.1 was used for analysis in shown in panel F.

Figure S2 Exemplary MALDI MSI images generated before (A) and after (B) missing value annotation and from reciprocal ratios (C-D). MSI Data was acquired at 80 µm using NEDC as matrix.

Figure S3 Ratio of glutamate to glutamine and Fe^{2+} abundance are co-enriched in the outer cortex of the COX10 KO (right 4 sections) and WT (left 4 sections) brain.

Figure S4 ROIs and UMAP scatter plots generated from non-ratio metabolite data. Panel A-I: Nine segmented ROIs generated UMAP and K-mean clustering analysis corresponding to clustered regions of 1-9. Panel J: Scatterplot of UMAP first 2 components (V1 vs V2) projecting the distribution and similarity of 9 segmented ROIs resulting in a incomplete and inconsistent ROIs among replicates. 5 LPE (Table S3) pixel data was used for UMAP analysis.

Figure S5 ROIs and UMAP scatter plots generated from metabolite ratio data. Panel A-I: Nine segmented ROIs generated UMAP and K-mean clustering analysis corresponding to clustered regions of 1-9. Panel J: Scatterplot of UMAP first 2 components (V1 vs V2) projecting the distribution and similarity of 9 segmented ROIs shows a distinct LPE profile between outer cortex (ROI 3) cortex (ROI 8) and ventral thalamus (ROI 5) striatum region(ROI2). Ratio of 5 LPE (Table S3) pixel data was used for UMAP.

Figure S6 Ratio images of NAA, NAAG and aspartate for UMAP-generated ROIs. Panel A-H: Ratio image of NAA to aspartate in 8 UMAP-segmented ROIs. Panel I-J: Ratio images of NAAG to NAA (I) and NAAG to aspartate in ROI 7 of UAMP segmented ROIs.

Figure S7 Images of NAAG and neurotransmitter related metabolites visualized in UMAP-generated ROI 7. Panel A: NAAG is enriched and elevated in in ROI 7–like region of COX 10 KO brain. Panel B-D: NAA,NAAG and glutamine are elevated in ROI 7 of COX 10 KO brain. Panel E: decreased level of aspartate in ROI 7 of COX10 KO; Panel F: Glutamate shows no change in ROI 7 of COX 10 KO compared to WT.

Figure S8 Pixel-by-pixel correlation of glutamine to glutamate ratio with a compendium of all detected metabolites and ratios exclusively in UMAP-generated ROI 7, comparing WT (A) to COX 10 KO (B) brain.

Only significant correlations with a spearman correlation coefficient of greater than 0.4 were presented in the figure.

Figure S9 UMAP using 5LPE ratios generated ROIs consistent with brain anatomy in two separate experiments with horizonal and sagittal brain sections. Panel A-B: Overlay of nine segmented ROIs generated from UMAP and K-mean clustering analysis in horizonal hemisphere sections (A) and sagittal brain sections (B). Panel C-D: Scatterplot of UMAP first 2 components (V1 vs V2) projecting the distribution and similarity of 9 segmented ROIs in horizonal (C) and sagittal sections (D). See Table S3 for the list of 5 LPEs.

References

1. Shimma, S. (2022). Mass Spectrometry Imaging. Mass Spectrom (Tokyo) *11*, A0102. 10.5702/massspectrometry.A0102.
2. Zhang, H., Delafield, D.G., and Li, L. (2023). Mass spectrometry imaging: the rise of spatially resolved single-cell omics. Nat Methods *20*, 327-330. 10.1038/s41592-023-01774-6.
3. Zhang, L., Liang, X., Takac, T., Komis, G., Li, X., Zhang, Y., Ovecka, M., Chen, Y., and Samaj, J. (2023). Spatial proteomics of vesicular trafficking: coupling mass spectrometry and imaging approaches in membrane biology. Plant Biotechnol J *21*, 250-269. 10.1111/pbi.13929.
4. Wang, J., Zhao, J., Nie, S., Xie, M., and Li, S. (2023). MALDI mass spectrometry in food carbohydrates analysis: A review of recent researches. Food Chem *399*, 133968. 10.1016/j.foodchem.2022.133968.
5. Soudah, T., Zoabi, A., and Margulis, K. (2023). Desorption electrospray ionization mass spectrometry imaging in discovery and development of novel therapies. Mass Spectrom Rev *42*, 751-778. 10.1002/mas.21736.
6. Sivanesan, I., Gopal, J., Hasan, N., and Muthu, M. (2023). A systematic assessment of matrix-assisted laser desorption/ionization time of flight mass spectrometry (MALDI-TOF MS) application for rapid identification of pathogenic microbes that affect food crops: delivered and future deliverables. RSC Adv *13*, 17297-17314. 10.1039/d3ra01633a.
7. Roncevic, A., Koruga, N., Soldo Koruga, A., Debeljak, Z., Roncevic, R., Turk, T., Kretic, D., Rotim, T., Krivdic Dupan, Z., Troha, D., et al. (2023). MALDI Imaging Mass Spectrometry of High-Grade Gliomas: A Review of Recent Progress and Future Perspective. Curr Issues Mol Biol *45*, 838-851. 10.3390/cimb45020055.
8. Moore, J.L., Patterson, N.H., Norris, J.L., and Caprioli, R.M. (2023). Prospective on Imaging Mass Spectrometry in Clinical Diagnostics. Mol Cell Proteomics, 100576. 10.1016/j.mcpro.2023.100576.
9. Liu, J., Hu, W., Han, Y., and Nie, H. (2023). Recent advances in mass spectrometry imaging of single cells. Anal Bioanal Chem *415*, 4093-4110. 10.1007/s00216-023-04774-9.
10. Li, D., Ouyang, Z., and Ma, X. (2023). Mass Spectrometry Imaging for Single-Cell or Subcellular Lipidomics: A Review of Recent Advancements and Future Development. Molecules *28*. 10.3390/molecules28062712.
11. Jiang, L.X., Yang, M., Wali, S.N., and Laskin, J. (2023). High-Throughput Mass Spectrometry Imaging of Biological Systems: Current Approaches and Future Directions. Trends Analyt Chem *163*. 10.1016/j.trac.2023.117055.
12. Ikegawa, M., Kakuda, N., Miyasaka, T., Toyama, Y., Nirasawa, T., Minta, K., and Hanrieder, J. (2023). Mass Spectrometry Imaging in Alzheimer's Disease. Brain Connect. 10.1089/brain.2022.0057.
13. Gorman, B.L., Torti, S.V., Torti, F.M., and Anderton, C.R. (2023). Mass spectrometry imaging of metals in tissues and cells: Methods and biological applications. Biochim Biophys Acta Gen Subj, 130329. 10.1016/j.bbagen.2023.130329.

14. Gitta, S., Mark, L., Szentpeteri, J.L., and Szabo, E. (2023). Lipid Changes in the Peri-Implantation Period with Mass Spectrometry Imaging: A Systematic Review. Life (Basel) *13*. 10.3390/life13010169.
15. Zou, Y., Tang, W., and Li, B. (2022). Mass spectrometry imaging and its potential in food microbiology. Int J Food Microbiol *371*, 109675. 10.1016/j.ijfoodmicro.2022.109675.
16. Zhao, Z., Ding, Y., Tran, L.J., Chai, G., and Lin, L. (2023). Innovative breakthroughs facilitated by single-cell multi-omics: manipulating natural killer cell functionality correlates with a novel subcategory of melanoma cells. Front Immunol *14*, 1196892. 10.3389/fimmu.2023.1196892.
17. Vos, D.R.N., Ellis, S.R., Balluff, B., and Heeren, R.M.A. (2021). Experimental and Data Analysis Considerations for Three-Dimensional Mass Spectrometry Imaging in Biomedical Research. Mol Imaging Biol *23*, 149-159. 10.1007/s11307-020-01541-5.
18. Verbeeck, N., Caprioli, R.M., and Van de Plas, R. (2020). Unsupervised machine learning for exploratory data analysis in imaging mass spectrometry. Mass Spectrom Rev *39*, 245-291. 10.1002/mas.21602.
19. Alexandrov, T. (2012). MALDI imaging mass spectrometry: statistical data analysis and current computational challenges. BMC Bioinformatics *13 Suppl 16*, S11. 10.1186/1471-2105-13-S16-S11.
20. Trede, D., Kobarg, J.H., Oetjen, J., Thiele, H., Maass, P., and Alexandrov, T. (2012). On the importance of mathematical methods for analysis of MALDI-imaging mass spectrometry data. J Integr Bioinform *9*, 189. 10.2390/biecoll-jib-2012-189.
21. Riches, S.F., Payne, G.S., Morgan, V.A., Sandhu, S., Fisher, C., Germuska, M., Collins, D.J., Thompson, A., and deSouza, N.M. (2009). MRI in the detection of prostate cancer: combined apparent diffusion coefficient, metabolite ratio, and vascular parameters. AJR Am J Roentgenol *193*, 1583-1591. 10.2214/AJR.09.2540.
22. Suhre, K., Wallaschofski, H., Raffler, J., Friedrich, N., Haring, R., Michael, K., Wasner, C., Krebs, A., Kronenberg, F., Chang, D., et al. (2011). A genome-wide association study of metabolic traits in human urine. Nat Genet *43*, 565-569. 10.1038/ng.837.
23. Illig, T., Gieger, C., Zhai, G., Romisch-Margl, W., Wang-Sattler, R., Prehn, C., Altmaier, E., Kastenmuller, G., Kato, B.S., Mewes, H.W., et al. (2010). A genome-wide perspective of genetic variation in human metabolism. Nat Genet *42*, 137-141. 10.1038/ng.507.
24. Gieger, C., Geistlinger, L., Altmaier, E., Hrabe de Angelis, M., Kronenberg, F., Meitinger, T., Mewes, H.W., Wichmann, H.E., Weinberger, K.M., Adamski, J., et al. (2008). Genetics meets metabolomics: a genome-wide association study of metabolite profiles in human serum. PLoS Genet *4*, e1000282. 10.1371/journal.pgen.1000282.
25. Petersen, A.K., Krumsiek, J., Wagele, B., Theis, F.J., Wichmann, H.E., Gieger, C., and Suhre, K. (2012). On the hypothesis-free testing of metabolite ratios in genome-wide and metabolome-wide association studies. BMC Bioinformatics *13*, 120. 10.1186/1471-2105-13-120.
26. Lassen, J.K., Wang, T., Nielsen, K.L., Hasselstrom, J.B., Johannsen, M., and Villesen, P. (2023). Large-Scale metabolomics: Predicting biological age using 10,133 routine untargeted LC-MS measurements. Aging Cell *22*, e13813. 10.1111/acel.13813.
27. Pang, Z., Zhou, G., Ewald, J., Chang, L., Hacariz, O., Basu, N., and Xia, J. (2022). Using MetaboAnalyst 5.0 for LC-HRMS spectra processing, multi-omics integration and covariate adjustment of global metabolomics data. Nat Protoc *17*, 1735-1761. 10.1038/s41596-022-00710-w.
28. Thompson, P.T., and Moseley, H.N.B. (2023). MESSES: Software for Transforming Messy Research Datasets into Clean Submissions to Metabolomics Workbench for Public Sharing. Metabolites *13*. 10.3390/metabo13070842.
29. Powell, C.D., and Moseley, H.N.B. (2023). The metabolomics workbench file status website: a metadata repository promoting FAIR principles of metabolomics data. BMC Bioinformatics *24*, 299. 10.1186/s12859-023-05423-9.
30. Sud, M., Fahy, E., Cotter, D., Azam, K., Vadivelu, I., Burant, C., Edison, A., Fiehn, O., Higashi, R., Nair, K.S., et al. (2016). Metabolomics Workbench: An international repository for metabolomics data and

metadata, metabolite standards, protocols, tutorials and training, and analysis tools. Nucleic Acids Res *44*, D463-470. 10.1093/nar/gkv1042.
31. Rodeiro, J., Vidana-Vila, E., Navarro, J., and Mallol, R. (2023). CloMet: A Novel Open-Source and Modular Software Platform That Connects Established Metabolomics Repositories and Data Analysis Resources. J Proteome Res *22*, 2540-2547. 10.1021/acs.jproteome.2c00602.
32. Du, X., Dastmalchi, F., Ye, H., Garrett, T.J., Diller, M.A., Liu, M., Hogan, W.R., Brochhausen, M., and Lemas, D.J. (2023). Evaluating LC-HRMS metabolomics data processing software using FAIR principles for research software. Metabolomics *19*, 11. 10.1007/s11306-023-01974-3.
33. Dekermanjian, J., Labeikovsky, W., Ghosh, D., and Kechris, K. (2021). MSCAT: A Machine Learning Assisted Catalog of Metabolomics Software Tools. Metabolites *11*. 10.3390/metabo11100678.
34. Plyushchenko, I.V., Fedorova, E.S., Potoldykova, N.V., Polyakovskiy, K.A., Glukhov, A.I., and Rodin, I.A. (2022). Omics Untargeted Key Script: R-Based Software Toolbox for Untargeted Metabolomics with Bladder Cancer Biomarkers Discovery Case Study. J Proteome Res *21*, 833-847. 10.1021/acs.jproteome.1c00392.
35. Misra, B.B. (2021). New software tools, databases, and resources in metabolomics: updates from 2020. Metabolomics *17*, 49. 10.1007/s11306-021-01796-1.
36. Chang, H.Y., Colby, S.M., Du, X., Gomez, J.D., Helf, M.J., Kechris, K., Kirkpatrick, C.R., Li, S., Patti, G.J., Renslow, R.S., et al. (2021). A Practical Guide to Metabolomics Software Development. Anal Chem *93*, 1912-1923. 10.1021/acs.analchem.0c03581.
37. O'Shea, K., and Misra, B.B. (2020). Software tools, databases and resources in metabolomics: updates from 2018 to 2019. Metabolomics *16*, 36. 10.1007/s11306-020-01657-3.
38. Adams, K.J., Pratt, B., Bose, N., Dubois, L.G., St John-Williams, L., Perrott, K.M., Ky, K., Kapahi, P., Sharma, V., MacCoss, M.J., et al. (2020). Skyline for Small Molecules: A Unifying Software Package for Quantitative Metabolomics. J Proteome Res *19*, 1447-1458. 10.1021/acs.jproteome.9b00640.
39. Misra, B.B. (2020). Open-Source Software Tools, Databases, and Resources for Single-Cell and Single-Cell-Type Metabolomics. Methods Mol Biol *2064*, 191-217. 10.1007/978-1-4939-9831-9_15.
40. Shahjaman, M., Rahman, M.R., Islam, T., Auwul, M.R., Moni, M.A., and Mollah, M.N.H. (2021). rMisbeta: A robust missing value imputation approach in transcriptomics and metabolomics data. Comput Biol Med *138*, 104911. 10.1016/j.compbiomed.2021.104911.
41. Wei, R., Wang, J., Su, M., Jia, E., Chen, S., Chen, T., and Ni, Y. (2018). Missing Value Imputation Approach for Mass Spectrometry-based Metabolomics Data. Sci Rep *8*, 663. 10.1038/s41598-017-19120-0.
42. Jin, Z., Kang, J., and Yu, T. (2018). Missing value imputation for LC-MS metabolomics data by incorporating metabolic network and adduct ion relations. Bioinformatics *34*, 1555-1561. 10.1093/bioinformatics/btx816.
43. Di Guida, R., Engel, J., Allwood, J.W., Weber, R.J., Jones, M.R., Sommer, U., Viant, M.R., and Dunn, W.B. (2016). Non-targeted UHPLC-MS metabolomic data processing methods: a comparative investigation of normalisation, missing value imputation, transformation and scaling. Metabolomics *12*, 93. 10.1007/s11306-016-1030-9.
44. Rieppo, J., Hyttinen, M.M., Jurvelin, J.S., and Helminen, H.J. (2004). Reference sample method reduces the error caused by variable cryosection thickness in Fourier transform infrared imaging. Appl Spectrosc *58*, 137-140. 10.1366/000370204322729577.
45. Lu, W., Park, N.R., TeSlaa, T., Jankowski, C.S.R., Samarah, L., McReynolds, M., Xing, X., Schembri, J., Woolf, M.T., Rabinowitz, J.D., and Davidson, S.M. (2023). Acidic Methanol Treatment Facilitates Matrix-Assisted Laser Desorption Ionization-Mass Spectrometry Imaging of Energy Metabolism. Anal Chem *95*, 14879-14888. 10.1021/acs.analchem.3c01875.
46. Knecht, K., Wiesmuller, K.H., Gnau, V., Jung, G., Meyermann, R., Todd, K.G., and Hamprecht, B. (2001). AMP deaminase in rat brain: localization in neurons and ependymal cells. J Neurosci Res *66*, 941-950. 10.1002/jnr.10059.

47. Andruchow, N.D., Konishi, K., Shatenstein, B., and Bohbot, V.D. (2017). A lower ratio of omega-6 to omega-3 fatty acids predicts better hippocampus-dependent spatial memory and cognitive status in older adults. Neuropsychology *31*, 724-734. 10.1037/neu0000373.
48. Southwell, N., Primiano, G., Nadkarni, V., Attarwala, N., Beattie, E., Miller, D., Alam, S., Liparulo, I., Shurubor, Y.I., Valentino, M.L., et al. (2023). A coordinated multiorgan metabolic response contributes to human mitochondrial myopathy. EMBO Mol Med *15*, e16951. 10.15252/emmm.202216951.
49. Bakker, N., Hickey, M., Shams, R., Rivera, C.F., Vlahos, J., Cense, H.A., Demirkiran, A., Ramkhelawon, B., and Houdijk, A.P. (2023). Oral omega-3 PUFA supplementation modulates inflammation in adipose tissue depots in morbidly obese women: A randomized trial. Nutrition *111*, 112055. 10.1016/j.nut.2023.112055.
50. Pinel, A., Rigaudiere, J.P., Morio, B., and Capel, F. (2021). Adipose Tissue Dysfunctions in Response to an Obesogenic Diet Are Reduced in Mice after Transgenerational Supplementation with Omega 3 Fatty Acids. Metabolites *11*. 10.3390/metabo11120838.
51. Portela, N.D., Galvan, C., Sanmarco, L.M., Bergero, G., Aoki, M.P., Cano, R.C., and Pesoa, S.A. (2023). Omega-3-Supplemented Fat Diet Drives Immune Metabolic Response in Visceral Adipose Tissue by Modulating Gut Microbiota in a Mouse Model of Obesity. Nutrients *15*. 10.3390/nu15061404.
52. Wall, R., Ross, R.P., Shanahan, F., O'Mahony, L., O'Mahony, C., Coakley, M., Hart, O., Lawlor, P., Quigley, E.M., Kiely, B., et al. (2009). Metabolic activity of the enteric microbiota influences the fatty acid composition of murine and porcine liver and adipose tissues. Am J Clin Nutr *89*, 1393-1401. 10.3945/ajcn.2008.27023.
53. Chiusolo, S., Bork, C.S., Gentile, F., Lundbye-Christensen, S., Harris, W.S., Schmidt, E.B., and De Caterina, R. (2023). Adipose tissue n-3/n-6 fatty acids ratios versus n-3 fatty acids fractions as predictors of myocardial infarction. Am Heart J *262*, 38-48. 10.1016/j.ahj.2023.03.019.
54. Rix, T.A., Dinesen, P., Lundbye-Christensen, S., Joensen, A.M., Riahi, S., Overvad, K., and Schmidt, E.B. (2022). Omega-3 fatty acids in adipose tissue and risk of atrial fibrillation. Eur J Clin Invest *52*, e13649. 10.1111/eci.13649.
55. Hertz, L., and Rothman, D.L. (2017). Glutamine-Glutamate Cycle Flux Is Similar in Cultured Astrocytes and Brain and Both Glutamate Production and Oxidation Are Mainly Catalyzed by Aspartate Aminotransferase. Biology (Basel) *6*. 10.3390/biology6010017.
56. Andersen, J.V., Schousboe, A., and Verkhratsky, A. (2022). Astrocyte energy and neurotransmitter metabolism in Alzheimer's disease: Integration of the glutamate/GABA-glutamine cycle. Prog Neurobiol *217*, 102331. 10.1016/j.pneurobio.2022.102331.
57. Pardo, B., Rodrigues, T.B., Contreras, L., Garzon, M., Llorente-Folch, I., Kobayashi, K., Saheki, T., Cerdan, S., and Satrustegui, J. (2011). Brain glutamine synthesis requires neuronal-born aspartate as amino donor for glial glutamate formation. J Cereb Blood Flow Metab *31*, 90-101. 10.1038/jcbfm.2010.146.
58. Szerb, J.C., and O'Regan, P.A. (1985). Effect of glutamine on glutamate release from hippocampal slices induced by high K+ or by electrical stimulation: interaction with different Ca2+ concentrations. J Neurochem *44*, 1724-1731. 10.1111/j.1471-4159.1985.tb07160.x.
59. Kantorova, E., Hnilicova, P., Bogner, W., Grendar, M., Grossmann, J., Kovacova, S., Heckova, E., Strasser, B., Cierny, D., Zelenak, K., and Kurca, E. (2022). Neurocognitive performance in relapsing-remitting multiple sclerosis patients is associated with metabolic abnormalities of the thalamus but not the hippocampus- GABA-edited 1H MRS study. Neurol Res *44*, 57-64. 10.1080/01616412.2021.1956282.
60. Kantorova, E., Hnilicova, P., Bogner, W., Grendar, M., Cierny, D., Heckova, E., Strasser, B., Ruzinak, R., Zelenak, K., and Kurca, E. (2021). Positivity of oligoclonal bands in the cerebrospinal fluid predisposed to metabolic changes and rearrangement of inhibitory/excitatory neurotransmitters in subcortical brain structures in multiple sclerosis. Mult Scler Relat Disord *52*, 102978. 10.1016/j.msard.2021.102978.

61. Limon, I.D., Angulo-Cruz, I., Sanchez-Abdon, L., and Patricio-Martinez, A. (2021). Disturbance of the Glutamate-Glutamine Cycle, Secondary to Hepatic Damage, Compromises Memory Function. Front Neurosci *15*, 578922. 10.3389/fnins.2021.578922.
62. Hangel, G., Cadrien, C., Lazen, P., Furtner, J., Lipka, A., Heckova, E., Hingerl, L., Motyka, S., Gruber, S., Strasser, B., et al. (2020). High-resolution metabolic imaging of high-grade gliomas using 7T-CRT-FID-MRSI. Neuroimage Clin *28*, 102433. 10.1016/j.nicl.2020.102433.
63. Yu, J., Guo, Y., Sun, M., Li, B., Zhang, Y., and Li, C. (2009). Iron is a potential key mediator of glutamate excitotoxicity in spinal cord motor neurons. Brain Res *1257*, 102-107. 10.1016/j.brainres.2008.12.030.
64. Burger, A., Kotze, M.J., Stein, D.J., Janse van Rensburg, S., and Howells, F.M. (2020). The relationship between measurement of in vivo brain glutamate and markers of iron metabolism: A proton magnetic resonance spectroscopy study in healthy adults. Eur J Neurosci *51*, 984-990. 10.1111/ejn.14583.
65. Peng Yu1, Ming Zhang1,2#, Hui Ding1, Xiaojing Di1, Peng Guan2, Shumin Wang1, Zhenhua Shi1, Dongyun Jiang1,2, Xianglin Duan1,2* and Yan-Zhong Chang1,2 (2015). Effect of Glutamate on Brain Iron Metabolism and the Regulation Mechanism. Journal of Drug Metabolism & Toxicology *6*, 1-10. 10.4172/2157-7609.1000190.
66. McGahan, M.C., Harned, J., Mukunnemkeril, M., Goralska, M., Fleisher, L., and Ferrell, J.B. (2005). Iron alters glutamate secretion by regulating cytosolic aconitase activity. Am J Physiol Cell Physiol *288*, C1117-1124. 10.1152/ajpcell.00444.2004.
67. Mittal, R.D., Pandey, A., Mittal, B., and Agarwal, K.N. (2003). Effect of latent iron deficiency on GABA and glutamate neuroreceptors in rat brain. Indian J Clin Biochem *18*, 111-116. 10.1007/BF02867677.
68. Sato, T., Shapiro, J.S., Chang, H.C., Miller, R.A., and Ardehali, H. (2022). Aging is associated with increased brain iron through cortex-derived hepcidin expression. Elife *11*. 10.7554/eLife.73456.
69. Wei, S., Shi, W., Li, M., and Gao, Q. (2014). Calorie restriction down-regulates expression of the iron regulatory hormone hepcidin in normal and D-galactose-induced aging mouse brain. Rejuvenation Res *17*, 19-26. 10.1089/rej.2013.1450.
70. Guo, A., Chen, Z., Li, F., and Luo, Q. (2022). Delineating regions of interest for mass spectrometry imaging by multimodally corroborated spatial segmentation. Gigascience *12*. 10.1093/gigascience/giad021.
71. Shi, W., Bell, S., Iyer, H., Brenden, C.K., Zhang, Y., Kim, S., Park, I., Bashir, R., Sweedler, J., and Vlasov, Y. (2022). Integrated silicon microfluidic chip for picoliter-scale analyte segmentation and microscale printing for mass spectrometry imaging. Lab Chip *23*, 72-80. 10.1039/d2lc00688j.
72. Guo, L., Liu, X., Zhao, C., Hu, Z., Xu, X., Cheng, K.K., Zhou, P., Xiao, Y., Shah, M., Xu, J., et al. (2022). iSegMSI: An Interactive Strategy to Improve Spatial Segmentation of Mass Spectrometry Imaging Data. Anal Chem *94*, 14522-14529. 10.1021/acs.analchem.2c01456.
73. Zou, Y., Tang, W., and Li, B. (2023). Spatial segmentation of mass spectrometry imaging data featuring selected principal components. Talanta *253*, 123958. 10.1016/j.talanta.2022.123958.
74. Baars, M.J.D., Sinha, N., Amini, M., Pieterman-Bos, A., van Dam, S., Ganpat, M.M.P., Lacle, M.M., Oldenburg, B., and Vercoulen, Y. (2021). MATISSE: a method for improved single cell segmentation in imaging mass cytometry. BMC Biol *19*, 99. 10.1186/s12915-021-01043-y.
75. Guo, L., Hu, Z., Zhao, C., Xu, X., Wang, S., Xu, J., Dong, J., and Cai, Z. (2021). Data Filtering and Its Prioritization in Pipelines for Spatial Segmentation of Mass Spectrometry Imaging. Anal Chem *93*, 4788-4793. 10.1021/acs.analchem.0c05242.
76. Hu, H., Yin, R., Brown, H.M., and Laskin, J. (2021). Spatial Segmentation of Mass Spectrometry Imaging Data by Combining Multivariate Clustering and Univariate Thresholding. Anal Chem *93*, 3477-3485. 10.1021/acs.analchem.0c04798.
77. Rothman, D.L., Behar, K.L., Prichard, J.W., and Petroff, O.A. (1997). Homocarnosine and the measurement of neuronal pH in patients with epilepsy. Magn Reson Med *38*, 924-929. 10.1002/mrm.1910380611.

78. Filipovic, D., Ivetic, V., Bozic, K., Nikolic, V., and Naumovic, N. (1993). [The effect of homocarnosine on neuronal activity during satiation and starvation]. Med Pregl *46*, 393-397.
79. Bondarenko, T.I., Krichevskaia, A.A., and Koshchii, G.N. (1985). [Homocarnosine in the brain of rats during cold adaptation]. Fiziol Zh SSSR Im I M Sechenova *71*, 333-336.
80. Kukharenko, R.I., Reva, A.D., and Rodina, S.L. (1990). [An increase in the brain homocarnosine level during alcohol intoxication]. Ukr Biokhim Zh (1978) *62*, 92-94.
81. Jalil, M.A., Begum, L., Contreras, L., Pardo, B., Iijima, M., Li, M.X., Ramos, M., Marmol, P., Horiuchi, M., Shimotsu, K., et al. (2005). Reduced N-acetylaspartate levels in mice lacking aralar, a brain- and muscle-type mitochondrial aspartate-glutamate carrier. J Biol Chem *280*, 31333-31339. 10.1074/jbc.M505286200.
82. Ohtsuka, C., and Takahashi, H. (1983). Brain function estimated from the ratio of glutamine to homocarnosine levels in cerebrospinal fluid. Brain Dev *5*, 509-511. 10.1016/s0387-7604(83)80084-9.
83. Enwonwu, C.O., and Worthington, B.S. (1973). Accumulation of histidine, 3-methylhistidine, and homocarnosine in the brains of protein-calorie deficient monkeys. J Neurochem *21*, 799-807. 10.1111/j.1471-4159.1973.tb07524.x.
84. Rather, A.A., and Chachoo, M.A. (2023). Robust correlation estimation and UMAP assisted topological analysis of omics data for disease subtyping. Comput Biol Med *155*, 106640. 10.1016/j.compbiomed.2023.106640.
85. ElKarami, B., Alkhateeb, A., Qattous, H., Alshomali, L., and Shahrrava, B. (2022). Multi-omics Data Integration Model Based on UMAP Embedding and Convolutional Neural Network. Cancer Inform *21*, 11769351221124205. 10.1177/11769351221124205.
86. Do, V.H., and Canzar, S. (2021). A generalization of t-SNE and UMAP to single-cell multimodal omics. Genome Biol *22*, 130. 10.1186/s13059-021-02356-5.
87. Kharel, P., Singhal, N.K., Mahendran, T., West, N., Croos, B., Rana, J., Smith, L., Freeman, E., Chattopadhyay, A., McDonough, J., and Basu, S. (2023). NAT8L mRNA oxidation is linked to neurodegeneration in multiple sclerosis. Cell Chem Biol *30*, 308-320 e305. 10.1016/j.chembiol.2023.02.007.
88. Uno, K., Miyanishi, H., Sodeyama, K., Fujiwara, T., Miyazaki, T., Muramatsu, S.I., and Nitta, A. (2019). Vulnerability to depressive behavior induced by overexpression of striatal Shati/Nat8l via the serotonergic neuronal pathway in mice. Behav Brain Res *376*, 112227. 10.1016/j.bbr.2019.112227.
89. Morland, C., and Nordengen, K. (2022). N-Acetyl-Aspartyl-Glutamate in Brain Health and Disease. Int J Mol Sci *23*. 10.3390/ijms23031268.

Table1 Spearman correlation of an unknown with ratio and non-ratio entities

Entity	Unknown [M-H] 375 23059
CPA 18:1	0 86090633
CPA 16:0	0 85862853
Docosahexaenoic_Acid	0 84761078
Palmitic_Acid	0 80091519
LPA 18:1	0 78455912
LPA 16:0	0 77663768
Oleic_Acid	0 77371792
PA 34:2	0 73231961
PA 36:3	0 72919804
Palmitoleic_Acid	0 72724047
CPA 18:0	0 70128825
LPE 16:0	0 69156441
PA 38:6	0 68799022
LPA 18:0	0 67264794
558. 4283	0 67163649
PE P 16:0	0 66456185
Linoleic_Acid	0 65773742
PI 36:2	0 65460109
LPA 18:2 / LPA 18:1	-0 53780801
PA 36:1 / LPA 18:1	-0 4549225
PA 36:4 / LPA 16:0	-0 42353603

Table 2 Brain glutamate to glutamine ratio positively correlates $FeCl_2$ using combined ratio and non-ratio pixel data and spearman correlation

Metabolite or Metabolite ratio	Gltamate / Glutamine
Glutamate / Glutamine	1
N-Acetylaspartate / Glutamine	0.69140746
Glutamate / Glucose	0.68318508
Aspartiate / Glutamine	0.617246741
Aspartate / Glucose	0.571634522
N-Acetylaspartate / Glucose	0.487447557
Glutathione / Glutamine	0.482704981
Glutamate / Malate	0.477826203
Glutamate / NAAG	0.418208761
Glutathione / Glucose	0.414914055
Glutamate / Taurine	0.408270132
Aspartate / NAAG	0.40560898
$FeCl_2$	0.40137113

Table S1 Brain glutamine to glutamate ratio negatively correlates $FeCl_2$ using combined ratio and non-ratio pixel data and spearman correlation

Metabolte or Metabolite ratio	Glutamine /Glutamate
Glutamine / Glutamate	1
NAA / Glutamine	-0.691412587
Glutamate / Glucose	-0.683182994
Aspartate / Glutamine	-0.617245759
Aspartate / Glucose	-0.571635589
NAA / Glucose	-0.48745363
Glutathione / Glutamine	-0.482699341
Glutamate / Malate	-0.477828273
Glutamate / NAAG	-0.418214673
Glutathione / Glucose	-0.414916374
Glutamate / Taurine	-0.408268788
Aspartate / NAAG	-0.40561461
$FeCl_2$	-0.40137478

Table S2 list of glutamate metabolism related metabolites for ratio generation and PCA segmentation of brain sections

m/z	Name
215.03279	Glucose+Cl
191.01973	Citrate
133.01425	Malate
132.03023	Aspartate
146.04588	Glutamate
145.06187	Glutamine
174.0408	N-Acetylaspartate
303.08339	N-Acetylaspartylglutamate
124.00739	Taurine
306.07653	Glutathione

Table S3 list of lyso PEs for ratio generation and PCA segmentation of brain sections

m/z	Name
478.2939	LPE 18:1
506.3252	LPE 20:1
500.2782	LPE 20:4
528.3095	LPE 22:4
524.2782	LPE 22:6

Table S4 Comparing correlation of neurotransmitter related metabolites and ratios in ROI7 of WT and KO brains

Entity Name	Spearman R square (WT)	Spearman R square (KO)
Glutamate/Glutamine	1	1
Glutamate/Glucose	0.852795869	0.678393963
Glutamate/Aspartic acid	0.801507737	0.558480678
Glutamate/N_Acetylaspartylglutamate	0.800125626	0.597592592
N_Acetylaspartate/N_Acetylaspartylglutamate	0.759938917	0.543231796
Taurine/N_Acetylaspartylglutamate	0.747279077	0.493250032
GSH/N_Acetylaspartylglutamate	0.725654702	0.534683985
Citrate/N_Acetylaspartylglutamate	0.670060429	0.3079266
Aspartate/N_Acetylaspartylglutamate	0.659178165	0.568779025
Glutamate/Malic acid	0.65035649	0.666255195
Taurine/Glutamine	0.648921859	0.554419257
Taurine/Glucose	0.644297546	0.452028615
Glutamine/N_Acetylaspartylglutamate	0.643225848	0.436576981
Malate/N_Acetylaspartylglutamate	0.624522126	0.441813603
Glutamate/N-Acetylaspartate	0.603496857	0.536109488
Glutamate/GSH	0.592151602	0.531586301
Taurine/GSH	0.567926578	0.282270798
Taurine/Malic acid	0.561595842	0.437632948
Glucose/N_Acetylaspartylglutamate	0.546762829	0.456179028
Taurine/Aspartate	0.543991912	0.289845889
N-Acetylaspartate/Glucose	0.485692311	0.460863975
Adenosine	0.48250312	0.339646908
Taurine/N-Acetylaspartate	0.480117014	0.263254553
Taurine/Citrate	0.444918698	0.56298861
Glutamine/Glucose	0.431762837	0.252386832
Glutamate	0.427270886	0.528188618
Glutamate/Citrate	0.414241714	0.592641696
Docosahexaenoic acid/Oleic acid	0.412424989	0.316780465
GSH/Glucose	0.409754542	0.418037354
N-Acetylaspartate/Glutamine	0.402130321	0.503623165
Glutamine/N-Acetylaspartate	-0.402121379	-0.503623105
Glucose/GSH	-0.409720091	-0.418038021
Oleic acid/Docosahexaenoic acid	-0.412418152	-0.316772044
Citrate/Glutamate	-0.41420686	-0.592642619
Glucose	-0.414832304	-0.247192996
Glucose/Glutamine	-0.431769617	-0.252433325
Cytidine	-0.440811865	-0.091933842
Citrate/Taurine	-0.444846276	-0.562985142
Glycerylphosphorylethanolamine	-0.446969716	-0.132695491
N-Acetylaspartate/Taurine	-0.480131641	-0.263259877
Glucose/Acetylaspartate	-0.485566843	-0.460873356
Aspartate/Taurine	-0.543994549	-0.2898528
N_Acetylaspartylglutamate//Glucose	-0.546773877	-0.456197823
Ribothymidine	-0.553276958	-0.345023745
Hypoxanthine	-0.55899857	-0.220084088
Threonate	-0.559486345	-0.21885935
Malate/Taurine	-0.56159942	-0.437638439
GSH/Taurine	-0.56793975	-0.28227912
Glutamyl_L_hydroxyproline	-0.576156273	-0.366588722
GSH/Glutamate	-0.592167807	-0.531584116
N-Acetylaspartate/Glutamate	-0.603520459	-0.536111131
N_Acetylaspartylglutamate/Malic acid	-0.624526454	-0.441825388
N_Acetylaspartylglutamate/Glutamine	-0.643220125	-0.43659667
Glucose/Taurine	-0.644270344	-0.452036941
Glutamine/Taurine	-0.64890671	-0.554426135
Malate/Glutamate	-0.650339314	-0.666263387
Inosine	-0.652470417	-0.328246954
N_Acetylaspartylglutamate	**-0.657380577**	**-0.463920793**
N_Acetylaspartylglutamate/Aspartic acid	**-0.659182447**	**-0.568791965**
N_Acetylaspartylglutamate/Citrate	-0.670054261	-0.307934844
N_Acetylaspartylglutamate/GSH	-0.725656919	-0.53469776
N_Acetylaspartylglutamate/Taurine	-0.747279393	-0.493256641
N_Acetylaspartylglutamate/N-Acetylaspartate	**-0.759938281**	**-0.543230626**
N_Acetylaspartylglutamate/Glutamate	-0.800114153	-0.59760264
Aspartate/Glutamate	-0.80148754	-0.55847547
Glucose/Glutamate	-0.852793526	-0.678396625
Glutamine/Glutamate	-0.999998899	-0.999999747

Figure 1

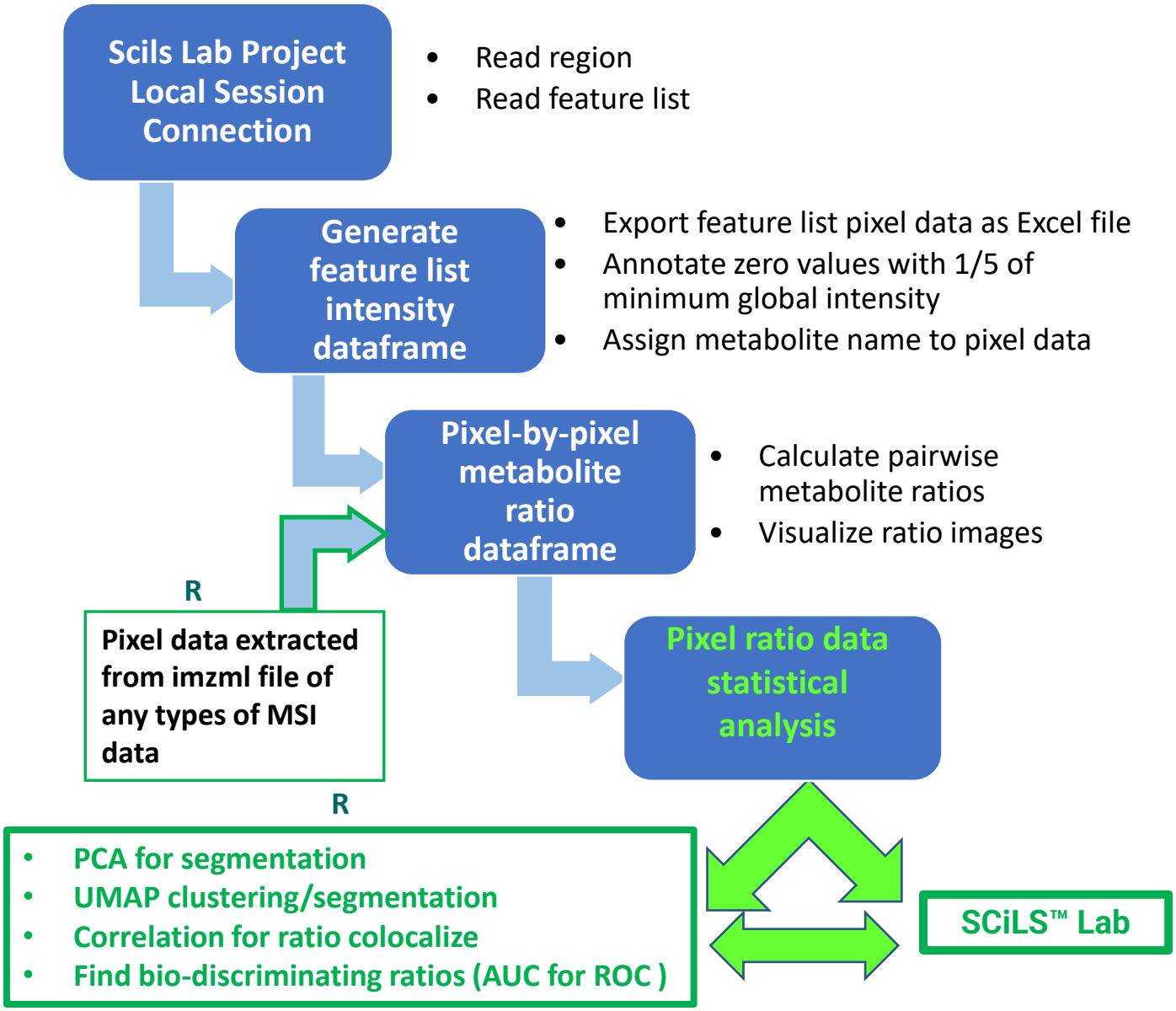
Scils Lab Project Local Session Connection
Read region
Read feature list
Generate feature list intensity dataframe
Export feature list pixel data as Excel file
Annotate zero values with 1/5 of minimum global intensity
Assign metabolite name to pixel data
Pixel-by-pixel metabolite ratio dataframe
Calculate pairwise metabolite ratios
Visualize ratio images
R
Pixel data extracted from imzml file of any types of MSI data
Pixel ratio data statistical analysis
R
PCA for segmentation
UMAP clustering/segmentation
Correlation for ratio colocalize
Find bio-discriminating ratios (AUC for ROC)
SCiLS™ Lab

Figure 2

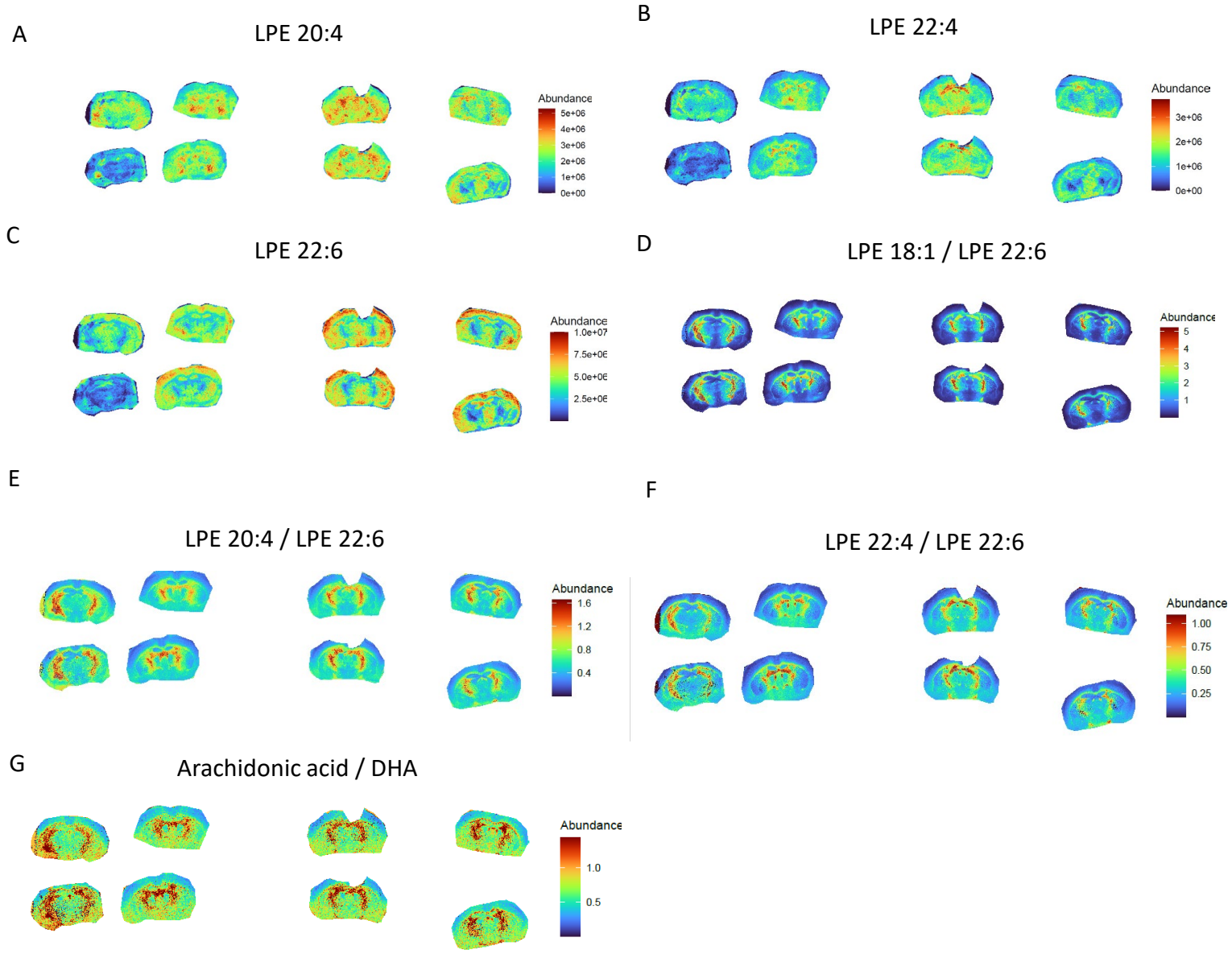
A
LPE 20:4
Abundance
5e+06
4e+06
3e+06
2e+06
1e+06
0e+00
B
LPE 22:4
Abundance
3e+06
2e+06
1e+06
0e+00
C
LPE 22:6
Abundance
1.0e+07
7.5e+06
5.0e+06
2.5e+06
D
LPE 18:1 / LPE 22:6
Abundance
5
4
3
2
1
E
LPE 20:4 / LPE 22:6
Abundance
1.6
1.2
0.8
0.4
F
LPE 22:4 / LPE 22:6
Abundance
1.00
0.75
0.50
0.25
G
Arachidonic acid / DHA
Abundance
1.0
0.5

Figure 3

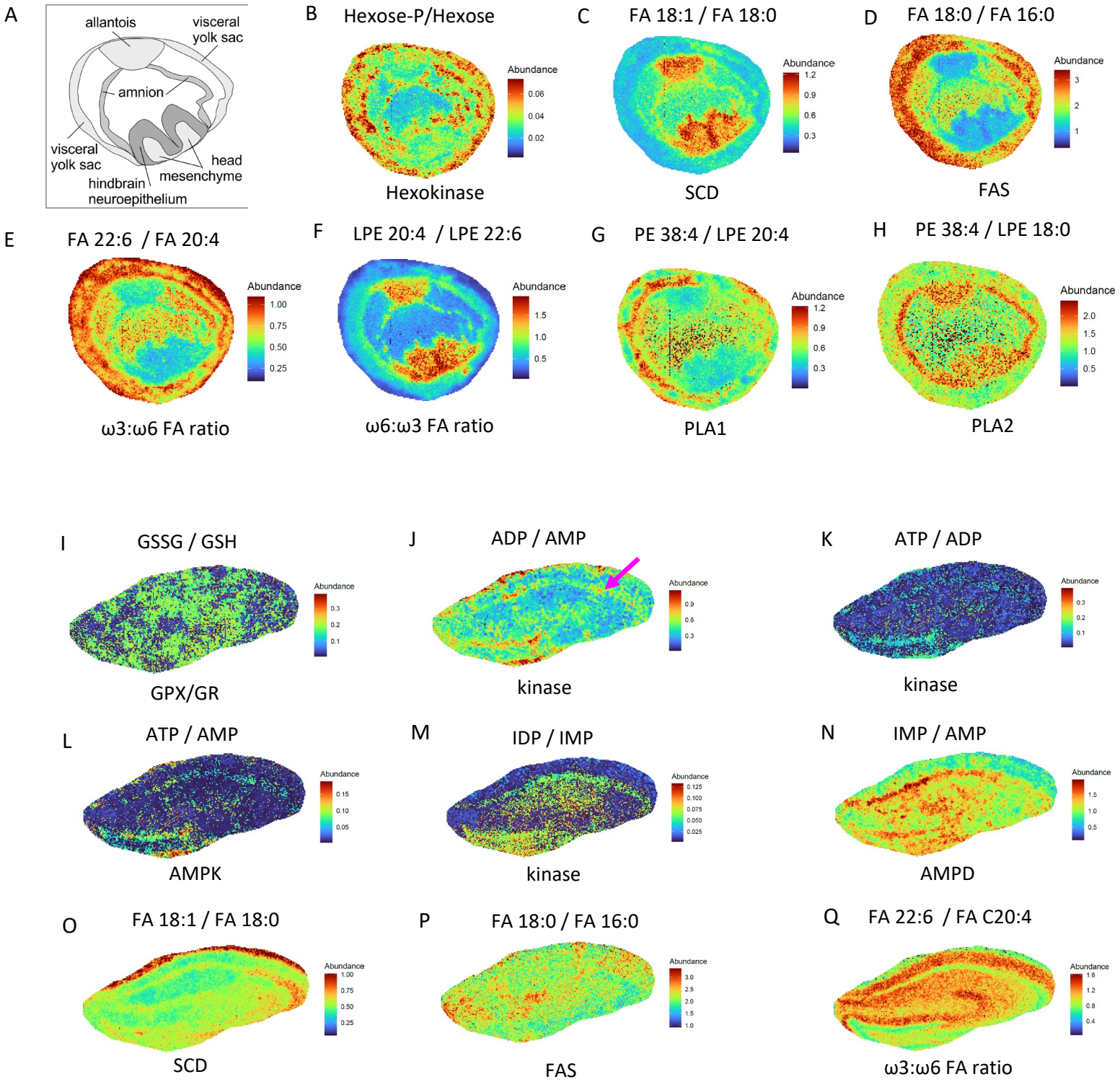
A
allantois
visceral yolk sac
amnion
visceral yolk sac
head mesenchyme
hindbrain neuroepithelium
B
Hexose-P/Hexose
Abundance
0.06
0.04
0.02
Hexokinase
C
FA 18:1 / FA 18:0
Abundance
1.2
0.9
0.6
0.3
SCD
D
FA 18:0 / FA 16:0
Abundance
3
2
1
FAS
E
FA 22:6 / FA 20:4
Abundance
1.00
0.75
0.50
0.25
ω3:ω6 FA ratio
F
LPE 20:4 / LPE 22:6
Abundance
1.5
1.0
0.5
ω6:ω3 FA ratio
G
PE 38:4 / LPE 20:4
Abundance
1.2
0.9
0.6
0.3
PLA1
H
PE 38:4 / LPE 18:0
Abundance
2.0
1.5
1.0
0.5
PLA2
I
GSSG / GSH
Abundance
0.3
0.2
0.1
GPX/GR
J
ADP / AMP
Abundance
0.9
0.6
0.3
kinase
K
ATP / ADP
Abundance
0.3
0.2
0.1
kinase
L
ATP / AMP
Abundance
0.15
0.10
0.05
AMPK
M
IDP / IMP
Abundance
0.125
0.100
0.075
0.050
0.025
kinase
N
IMP / AMP
Abundance
1.5
1.0
0.5
AMPD
O
FA 18:1 / FA 18:0
Abundance
1.00
0.75
0.50
0.25
SCD
P
FA 18:0 / FA 16:0
Abundance
3.0
2.5
2.0
1.5
1.0
FAS
Q
FA 22:6 / FA C20:4
Abundance
1.6
1.2
0.8
0.4
ω3:ω6 FA ratio

Figure 4

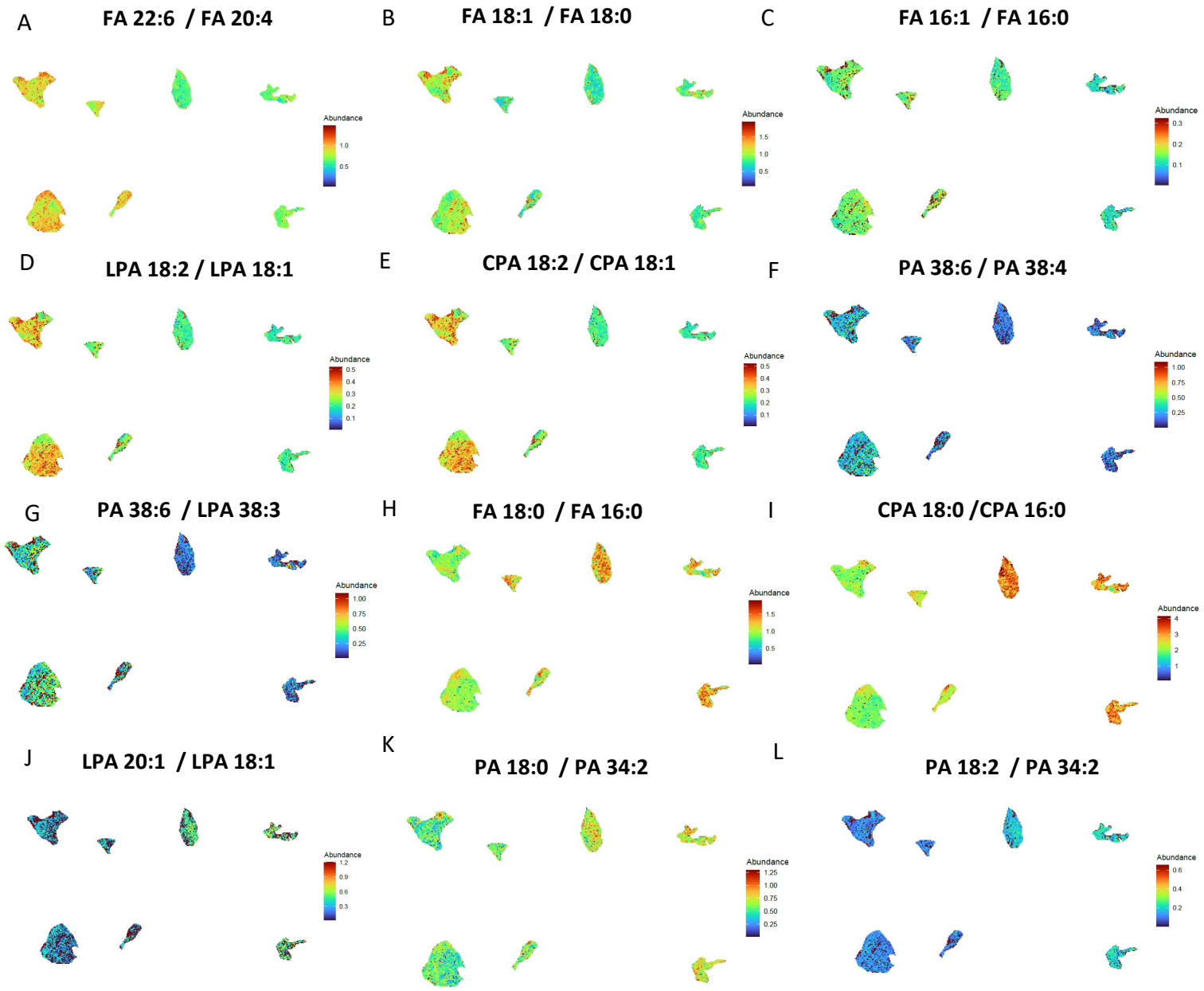
A
FA 22:6 / FA 20:4
Abundance
1.0
0.5
B
FA 18:1 / FA 18:0
Abundance
1.5
1.0
0.5
C
FA 16:1 / FA 16:0
Abundance
0.3
0.2
0.1
D
LPA 18:2 / LPA 18:1
Abundance
0.5
0.4
0.3
0.2
0.1
E
CPA 18:2 / CPA 18:1
Abundance
0.5
0.4
0.3
0.2
0.1
F
PA 38:6 / PA 38:4
Abundance
1.00
0.75
0.50
0.25
G
PA 38:6 / LPA 38:3
Abundance
1.00
0.75
0.50
0.25
H
FA 18:0 / FA 16:0
Abundance
1.5
1.0
0.5
I
CPA 18:0 /CPA 16:0
Abundance
4
3
2
1
J
LPA 20:1 / LPA 18:1
Abundance
1.2
0.9
0.6
0.3
K
PA 18:0 / PA 34:2
Abundance
1.25
1.00
0.75
0.50
0.25
L
PA 18:2 / PA 34:2
Abundance
0.6
0.4
0.2

Figure 5

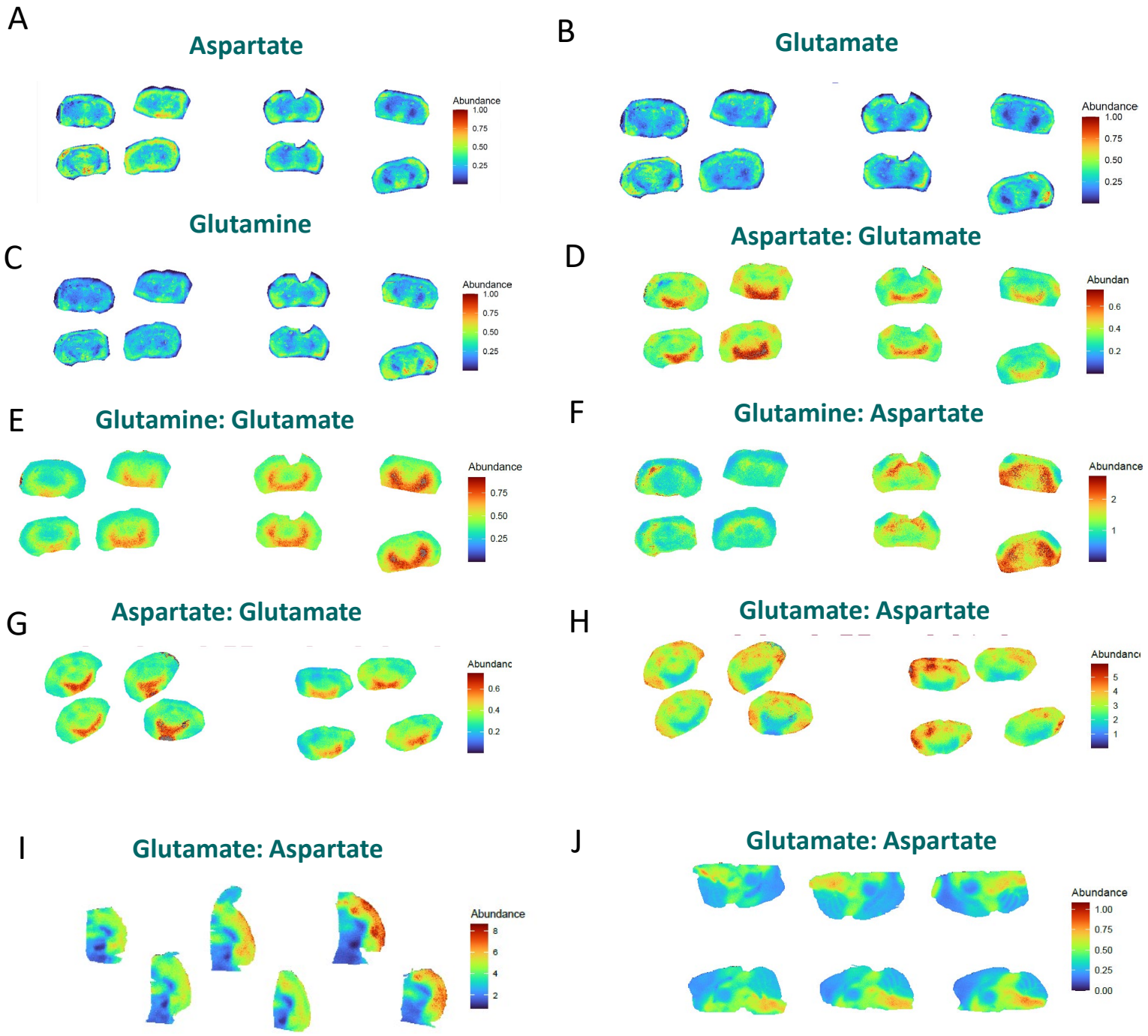
A
Aspartate
Abundance
1.00
0.75
0.50
0.25
B
Glutamate
Abundance
1.00
0.75
0.50
0.25
C
Glutamine
Abundance
1.00
0.75
0.50
0.25
D
Aspartate: Glutamate
Abundan
0.6
0.4
0.2
E
Glutamine: Glutamate
Abundance
0.75
0.50
0.25
F
Glutamine: Aspartate
Abundance
2
1
G
Aspartate: Glutamate
Abundanc
0.6
0.4
0.2
H
Glutamate: Aspartate
Abundanc
5
4
3
2
1
I
Glutamate: Aspartate
Abundance
8
6
4
2
J
Glutamate: Aspartate
Abundance
1.00
0.75
0.50
0.25
0.00

Figure 6

A **10 Glutamate Metabolites**

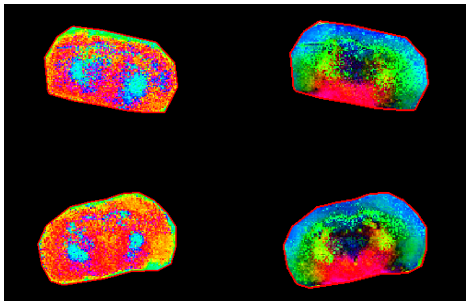

B **5 phospholipids (-PEs)**

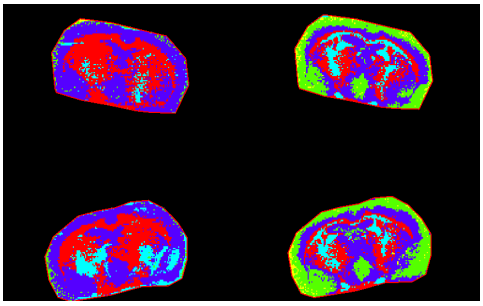

Ratio: **-** **+** **-** **+**

Figure 7

A

Asp :Gln

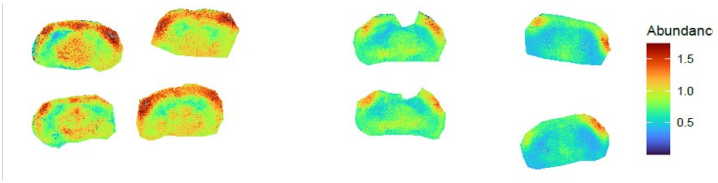

B

Homocarnosine: Asp

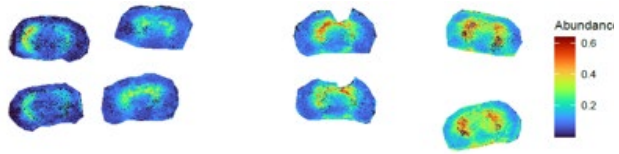

C

Homocarnosine: Gln

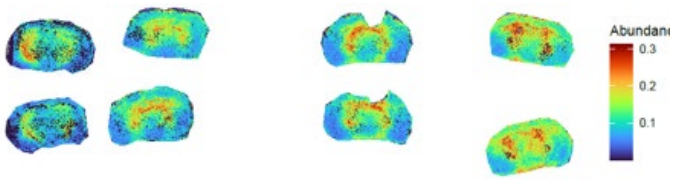

D

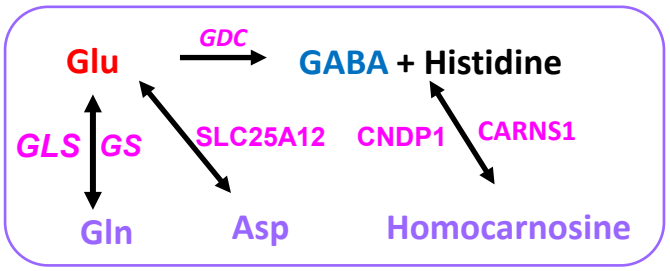

Homocarnosine

E

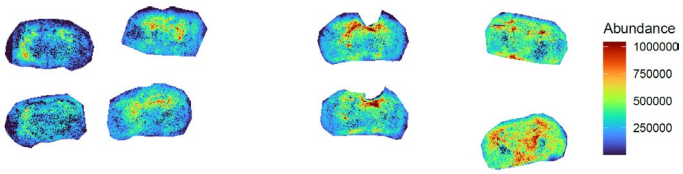

F

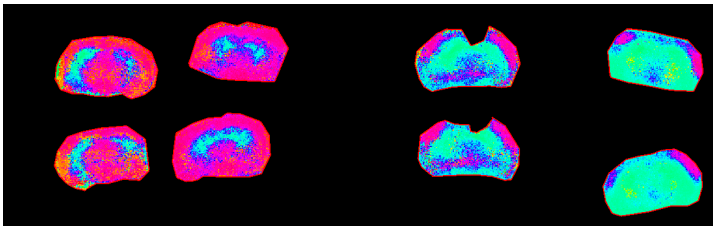

G

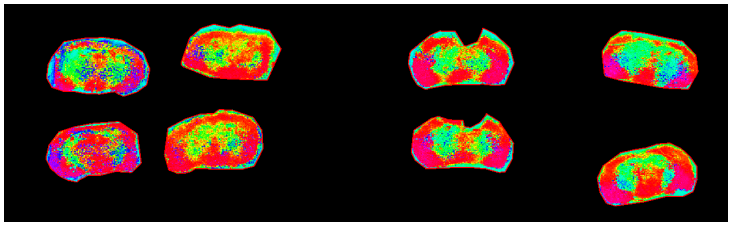

Figure 8

A

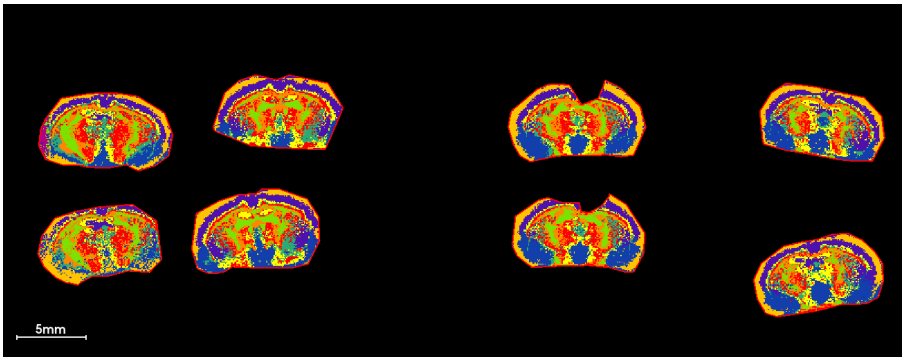

B

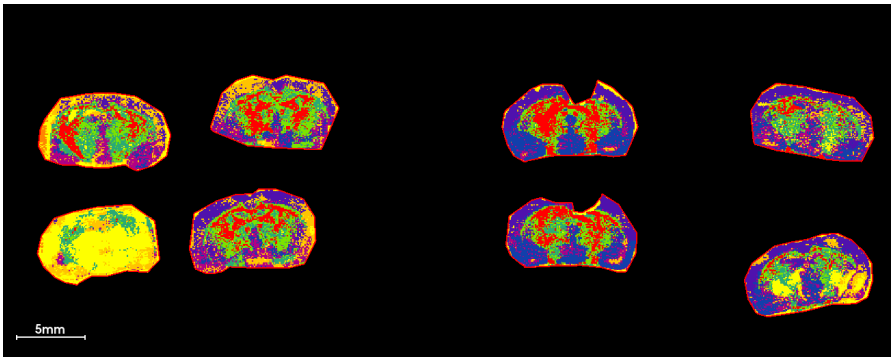

Figure S1

A

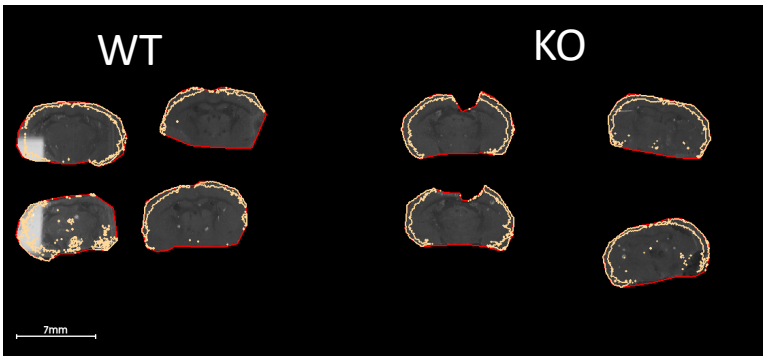

B

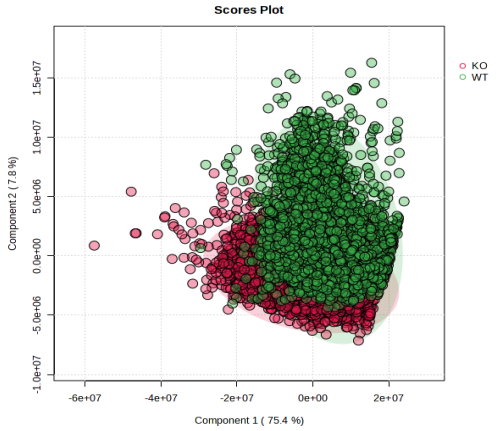

C

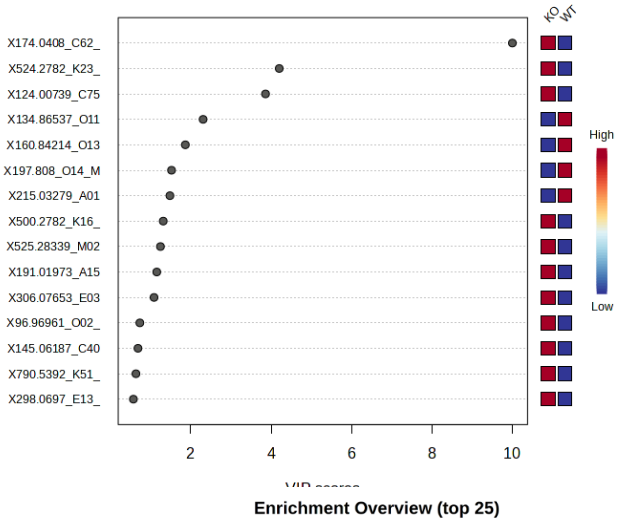

D

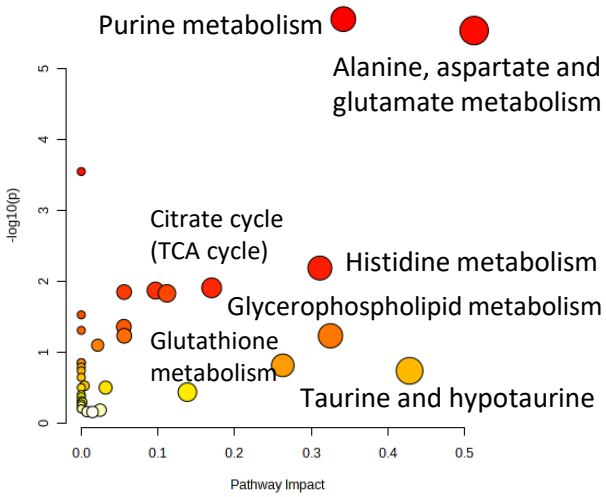

E

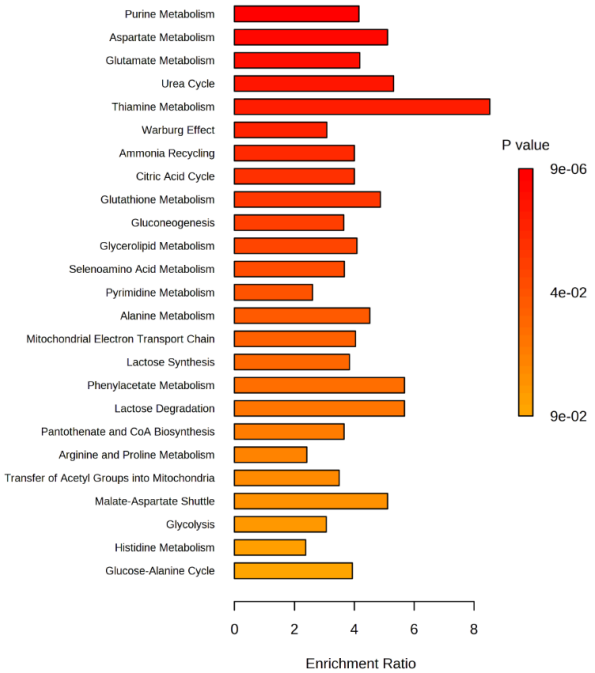

F

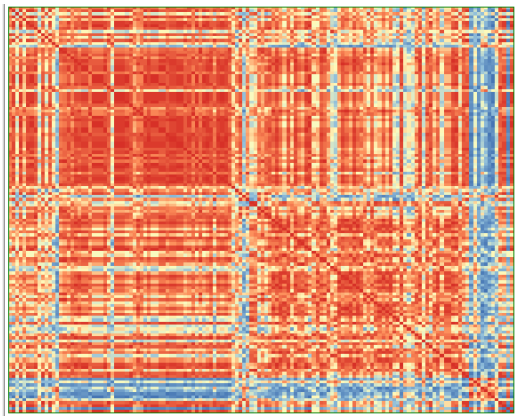

Figure S2

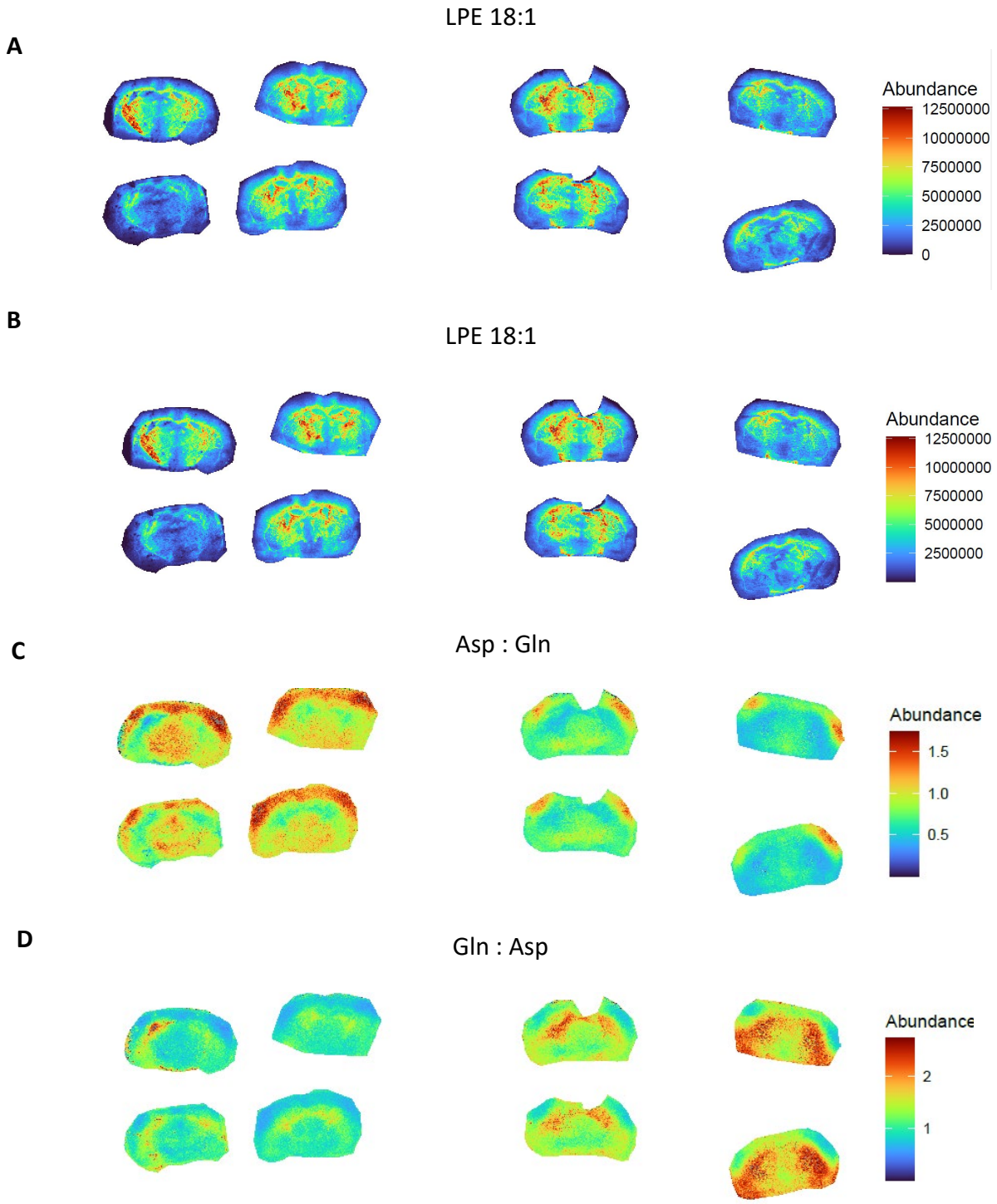
A
LPE 18:1
Abundance
12500000
10000000
7500000
5000000
2500000
0
B
LPE 18:1
Abundance
12500000
10000000
7500000
5000000
2500000
C
Asp : Gln
Abundance
1.5
1.0
0.5
D
Gln : Asp
Abundance
2
1

Figure S3

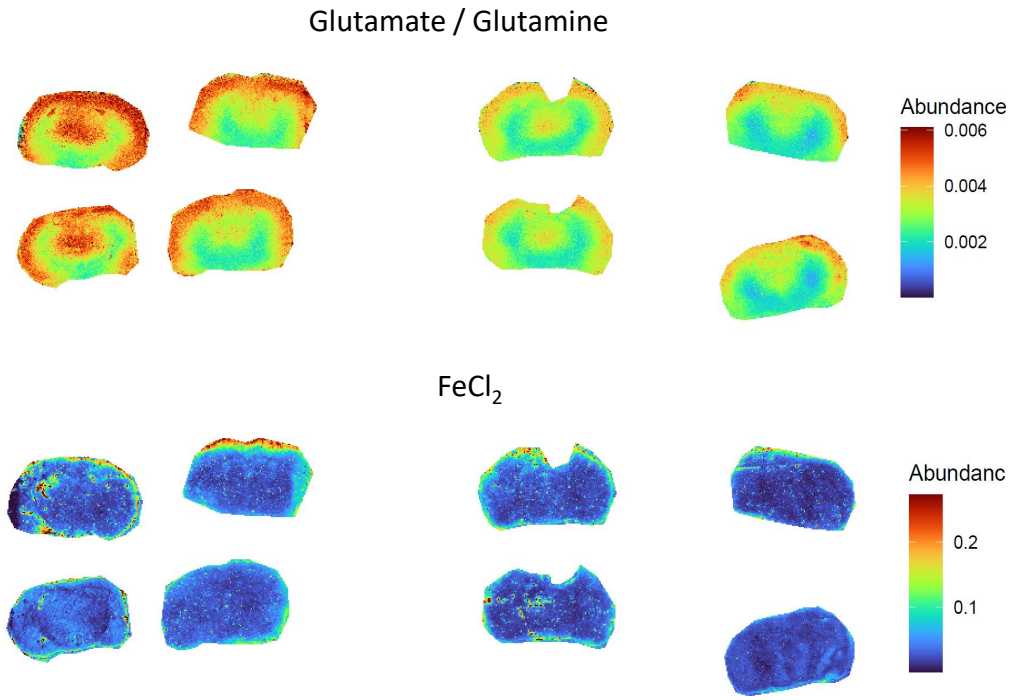
Glutamate / Glutamine
Abundance
0.006
0.004
0.002
FeCl2
Abundanc
0.2
0.1

Figure S4

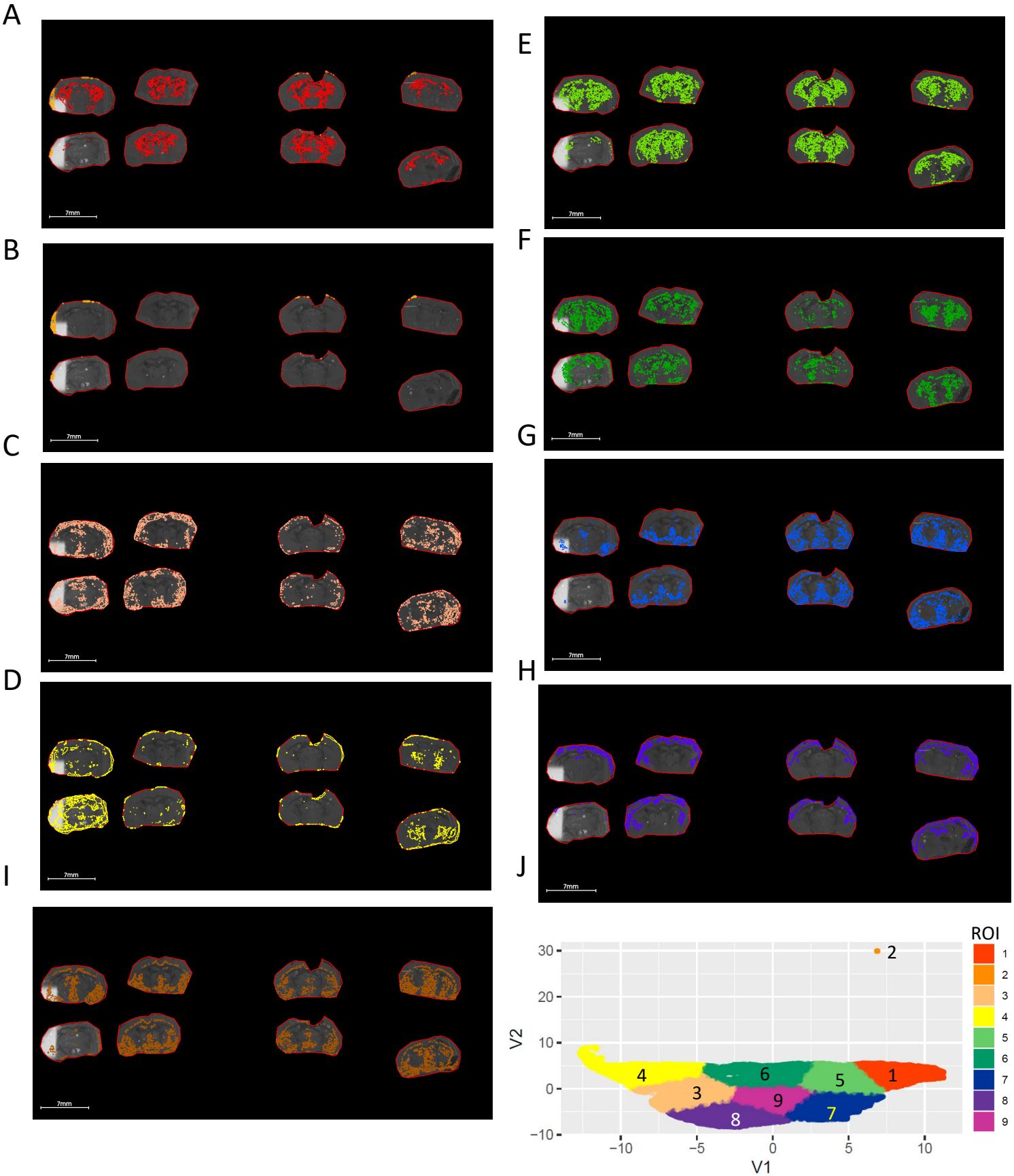

Figure S5

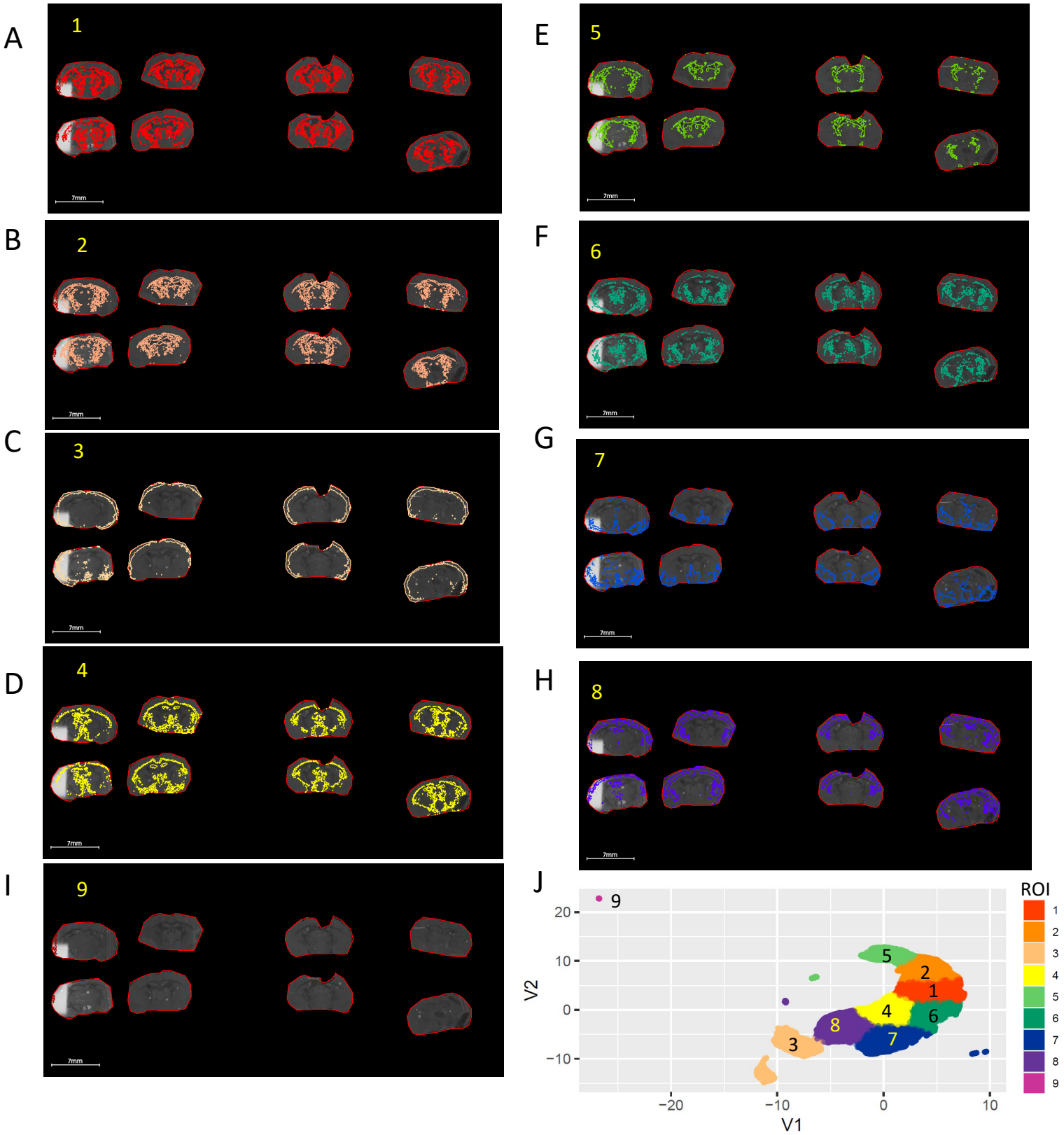

Figure S6

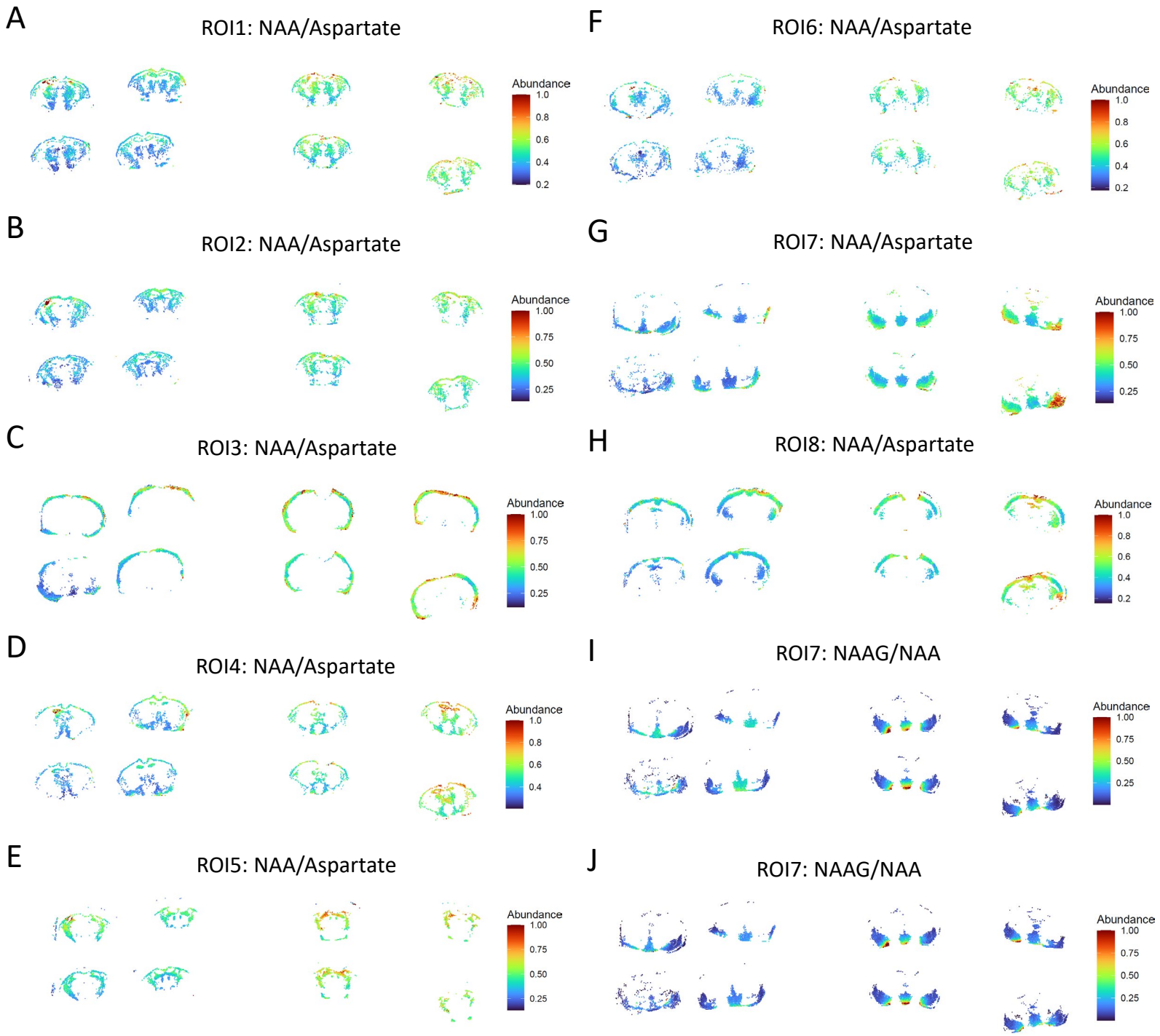
A
ROI1: NAA/Aspartate
Abundance
1.0
0.8
0.6
0.4
0.2
B
ROI2: NAA/Aspartate
Abundance
1.00
0.75
0.50
0.25
C
ROI3: NAA/Aspartate
Abundance
1.00
0.75
0.50
0.25
D
ROI4: NAA/Aspartate
Abundance
1.0
0.8
0.6
0.4
E
ROI5: NAA/Aspartate
Abundance
1.00
0.75
0.50
0.25
F
ROI6: NAA/Aspartate
Abundance
1.0
0.8
0.6
0.4
0.2
G
ROI7: NAA/Aspartate
Abundance
1.00
0.75
0.50
0.25
H
ROI8: NAA/Aspartate
Abundance
1.0
0.8
0.6
0.4
0.2
I
ROI7: NAAG/NAA
Abundance
1.00
0.75
0.50
0.25
J
ROI7: NAAG/NAA
Abundance
1.00
0.75
0.50
0.25

Figure S7

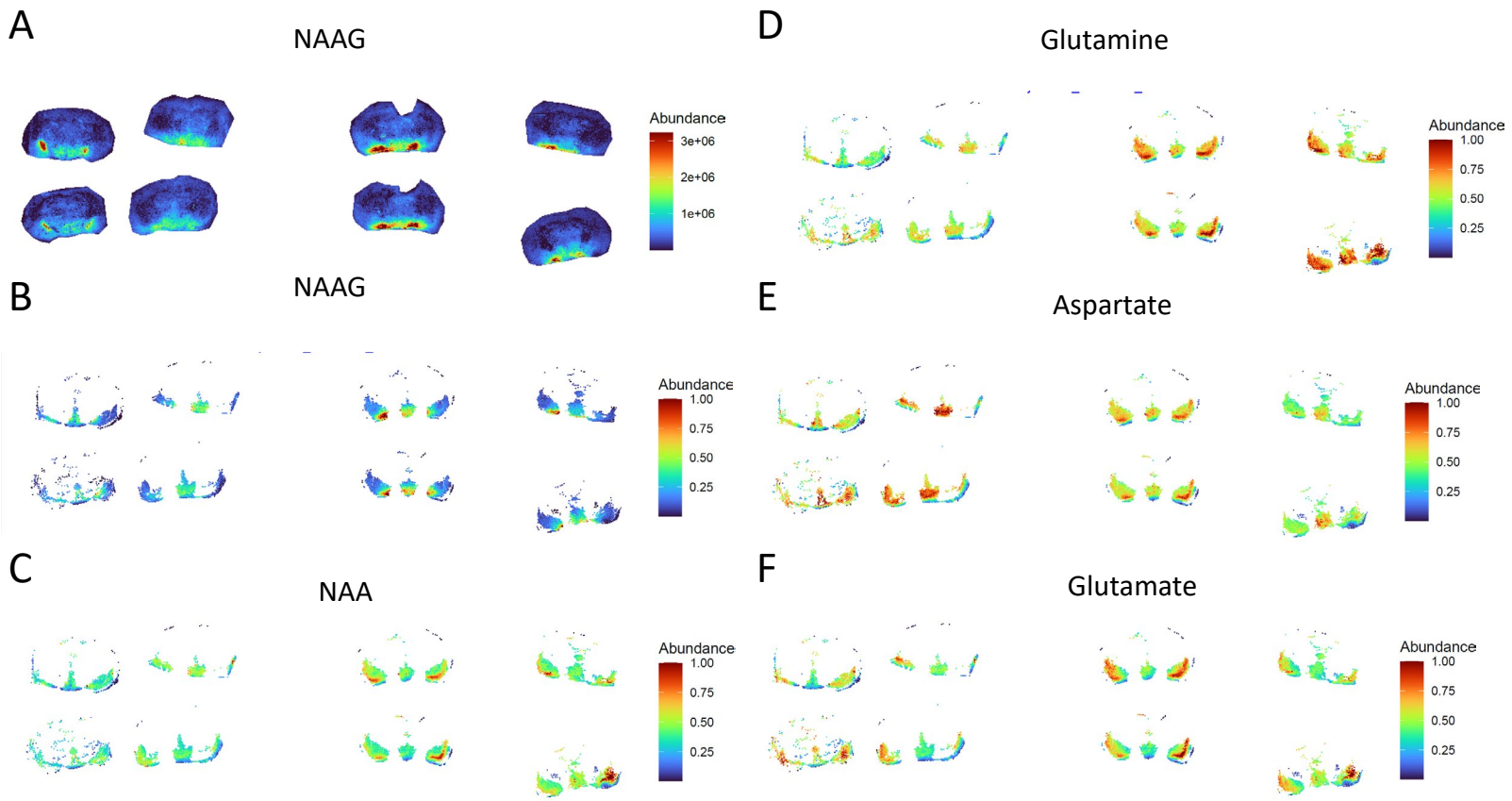
A
NAAG
Abundance
3e+06
2e+06
1e+06
B
NAAG
Abundance
1.00
0.75
0.50
0.25
C
NAA
Abundance
1.00
0.75
0.50
0.25
D
Glutamine
Abundance
1.00
0.75
0.50
0.25
E
Aspartate
Abundance
1.00
0.75
0.50
0.25
F
Glutamate
Abundance
1.00
0.75
0.50
0.25

Figure S8

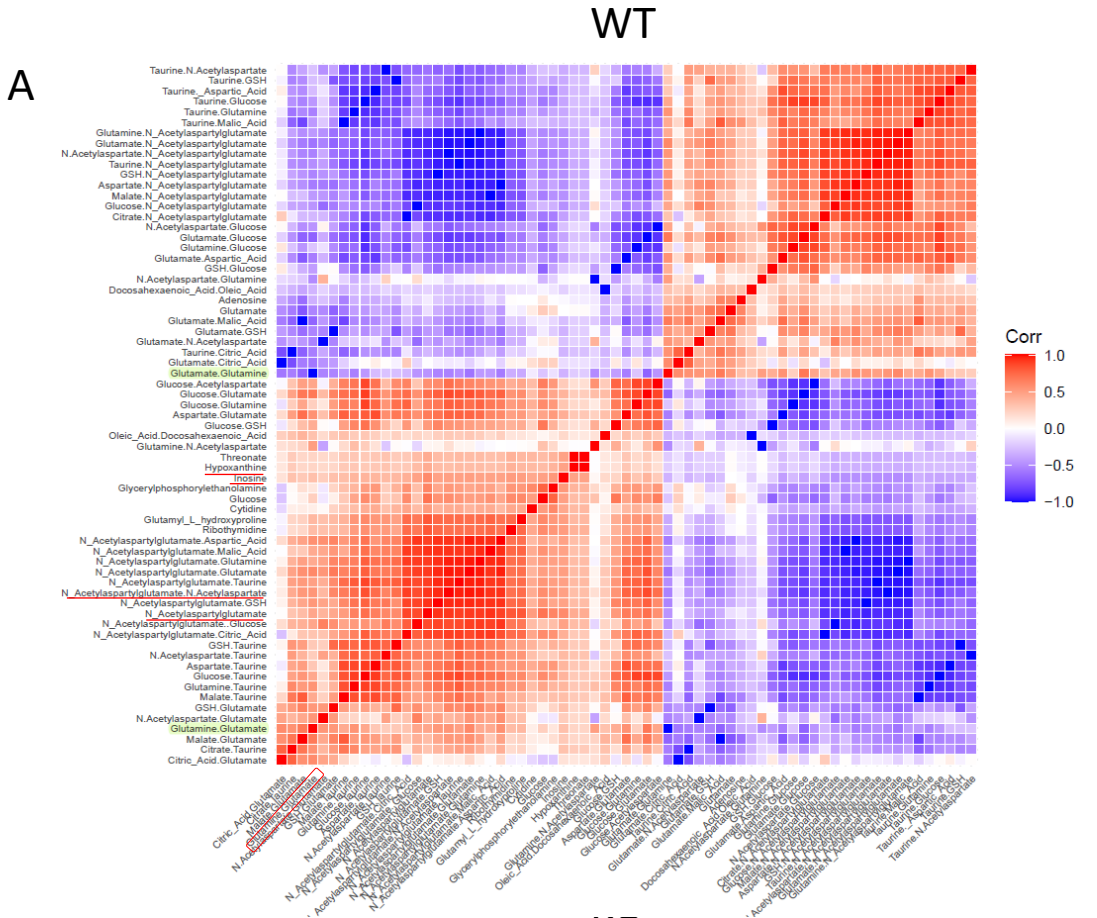

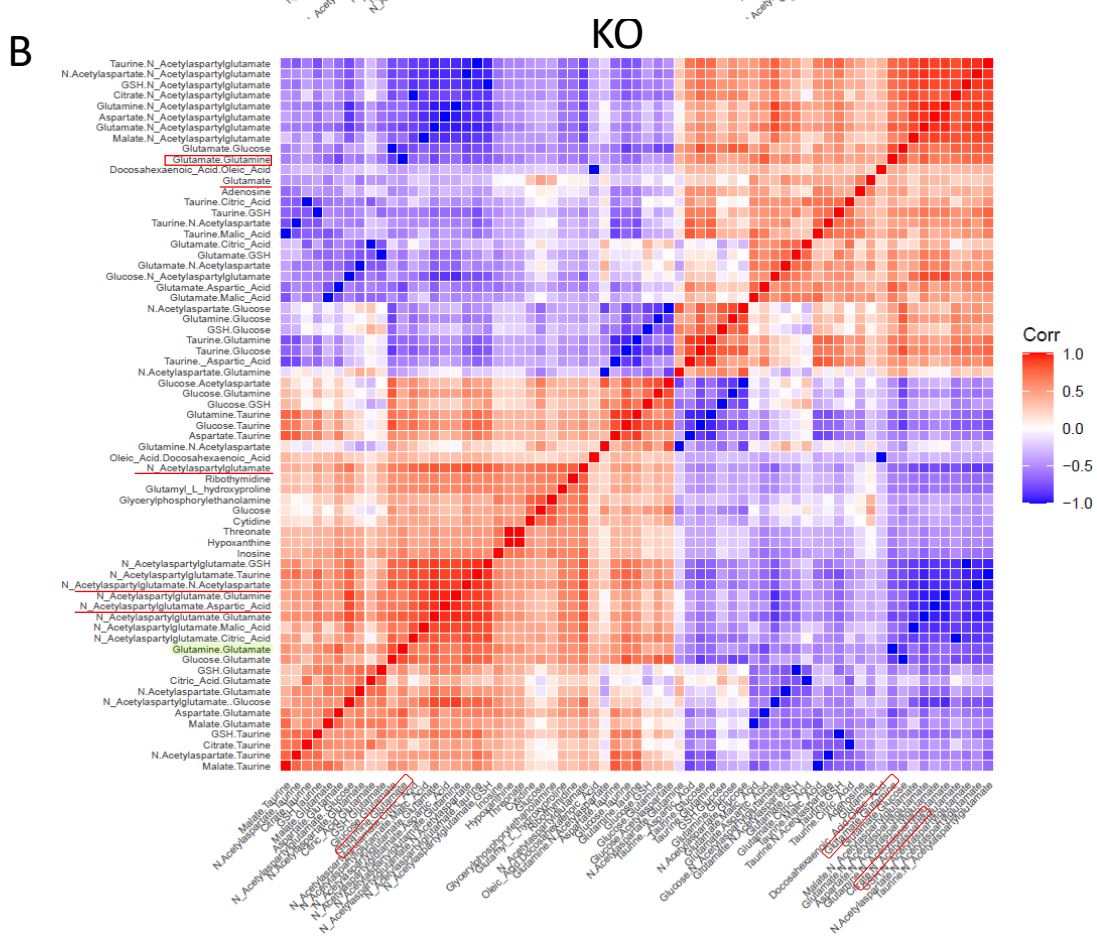

Fig S9

A

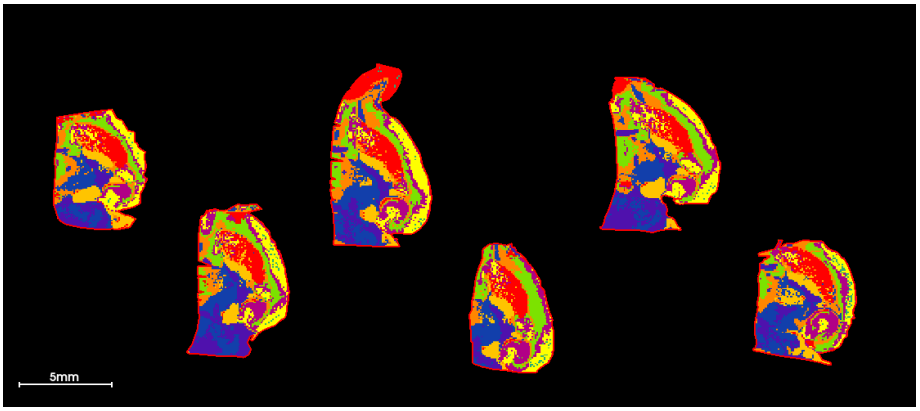
5mm

B

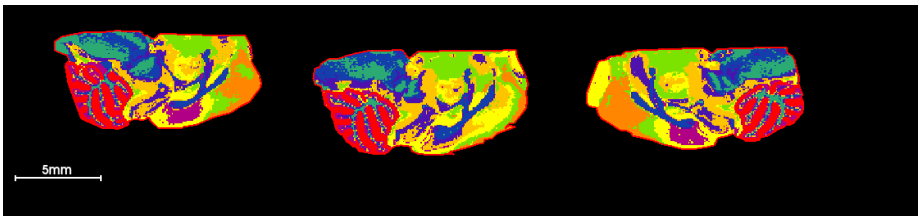
5mm

C

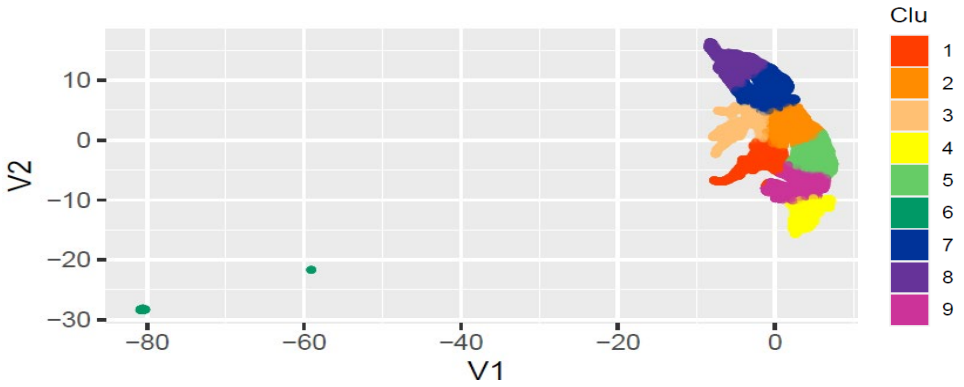
Clu
1
2
3
4
5
6
7
8
9
V2
10
0
−10
−20
−30
−80
−60
−40
−20
0
V1

D

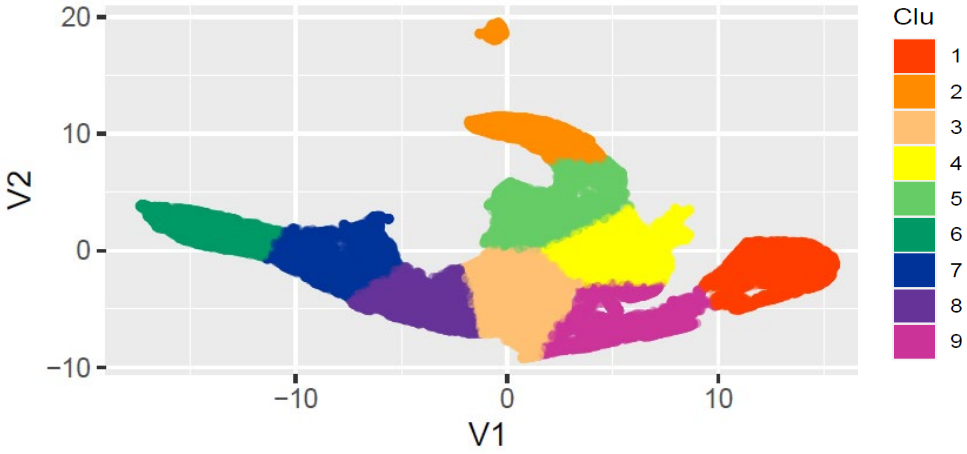
Clu
1
2
3
4
5
6
7
8
9
V2
20
10
0
−10
−10
0
10
V1